Observational Hertzsprung-Russell diagrams

Babusiaux, C.; van Leeuwen, F.; Barstow, M. A.; Cayuso, Jordi; Vallenari, A.; Lindstrøm, Hans Erik Peter; Bossini, D.; Bressan, Rodrigo A; Prusti, T.; de Bruijne, JHJ; Ulla, Anna; Taylor, MB; Vogt, S.; Essen, C. von; Yoldas, A.; Zerjal, M.; Zwitter, Tomaz

Published in:
Astronomy & Astrophysics

DOI:
10.1051/0004-6361/201832843

Publication date:
2018

Document version
Publisher's PDF, also known as Version of record

A&A 616, A10 (2018)
https://doi.org/10.1051/0004-6361/201832843

Astronomy & Astrophysics

Special issue

Gaia Data Release 2

Gaia Data Release 2

Observational Hertzsprung-Russell diagrams★

Gaia Collaboration, C. Babusiaux[1,2,★★], F. van Leeuwen[3], M. A. Barstow[4], C. Jordi[5], A. Vallenari[6], D. Bossini[6], A. Bressan[7], T. Cantat-Gaudin[6,5], M. van Leeuwen[3], A. G. A. Brown[8], T. Prusti[9], J. H. J. de Bruijne[9], C. A. L. Bailer-Jones[10], M. Biermann[11], D. W. Evans[3], L. Eyer[12], F. Jansen[13], S. A. Klioner[14], U. Lammers[15], L. Lindegren[16], X. Luri[5], F. Mignard[17], C. Panem[18], D. Pourbaix[19,20], S. Randich[21], P. Sartoretti[2], H. I. Siddiqui[22], C. Soubiran[23], N. A. Walton[3], F. Arenou[2], U. Bastian[11], M. Cropper[24], R. Drimmel[25], D. Katz[2], M. G. Lattanzi[25], J. Bakker[15], C. Cacciari[26], J. Castañeda[5], L. Chaoul[18], N. Cheek[27], F. De Angeli[3], C. Fabricius[5], R. Guerra[15], B. Holl[12], E. Masana[5], R. Messineo[28], N. Mowlavi[12], K. Nienartowicz[29], P. Panuzzo[2], J. Portell[5], M. Riello[3], G. M. Seabroke[24], P. Tanga[17], F. Thévenin[17], G. Gracia-Abril[30,11], G. Comoretto[22], M. Garcia-Reinaldos[15], D. Teyssier[22], M. Altmann[11,31], R. Andrae[10], M. Audard[12], I. Bellas-Velidis[32], K. Benson[24], J. Berthier[33], R. Blomme[34], P. Burgess[3], G. Busso[3], B. Carry[17,33], A. Cellino[25], G. Clementini[26], M. Clotet[5], O. Creevey[17], M. Davidson[35], J. De Ridder[36], L. Delchambre[37], A. Dell'Oro[21], C. Ducourant[23], J. Fernández-Hernández[38], M. Fouesneau[10], Y. Frémat[34], L. Galluccio[17], M. García-Torres[39], J. González-Núñez[27,40], J. J. González-Vidal[5], E. Gosset[37,20], L. P. Guy[29,41], J.-L. Halbwachs[42], N. C. Hambly[35], D. L. Harrison[3,43], J. Hernández[15], D. Hestroffer[33], S. T. Hodgkin[3], A. Hutton[44], G. Jasniewicz[45], A. Jean-Antoine-Piccolo[18], S. Jordan[11], A. J. Korn[46], A. Krone-Martins[47], A. C. Lanzafame[48,49], T. Lebzelter[50], W. Löffler[11], M. Manteiga[51,52], P. M. Marrese[53,54], J. M. Martín-Fleitas[44], A. Moitinho[47], A. Mora[44], K. Muinonen[55,56], J. Osinde[57], E. Pancino[21,54], T. Pauwels[34], J.-M. Petit[58], A. Recio-Blanco[17], P. J. Richards[59], L. Rimoldini[29], A. C. Robin[58], L. M. Sarro[60], C. Siopis[19], M. Smith[24], A. Sozzetti[25], M. Süveges[10], J. Torra[5], W. van Reeven[44], U. Abbas[25], A. Abreu Aramburu[61], S. Accart[62], C. Aerts[36,63], G. Altavilla[53,54,26], M. A. Álvarez[51], R. Alvarez[15], J. Alves[50], R. I. Anderson[64,12], A. H. Andrei[65,66,31], E. Anglada Varela[38], E. Antiche[5], T. Antoja[9,5], B. Arcay[51], T. L. Astraatmadja[10,67], N. Bach[44], S. G. Baker[24], L. Balaguer-Núñez[5], P. Balm[22], C. Barache[31], C. Barata[47], D. Barbato[68,25], F. Barblan[12], P. S. Barklem[46], D. Barrado[69], M. Barros[47], S. Bartholomé Muñoz[5], J.-L. Bassilana[62], U. Becciani[49], M. Bellazzini[26], A. Berihuete[70], S. Bertone[25,31,71], L. Bianchi[72], O. Bienaymé[42], S. Blanco-Cuaresma[12,23,73], T. Boch[42], C. Boeche[6], A. Bombrun[74], R. Borrachero[5], S. Bouquillon[31], G. Bourda[23], A. Bragaglia[26], L. Bramante[28], M. A. Breddels[75], N. Brouillet[23], T. Brüsemeister[11], E. Brugaletta[49], B. Bucciarelli[25], A. Burlacu[18], D. Busonero[25], A. G. Butkevich[14], R. Buzzi[25], E. Caffau[2], R. Cancelliere[76], G. Cannizzaro[77,63], R. Carballo[78], T. Carlucci[31], J. M. Carrasco[5], L. Casamiquela[5], M. Castellani[53], A. Castro-Ginard[5], P. Charlot[23], L. Chemin[79], A. Chiavassa[17], G. Cocozza[26], G. Costigan[8], S. Cowell[3], F. Crifo[2], M. Crosta[25], C. Crowley[74], J. Cuypers[†34], C. Dafonte[51], Y. Damerdji[37,80], A. Dapergolas[32], P. David[33], M. David[81], P. de Laverny[17], F. De Luise[82], R. De March[28], D. de Martino[83], R. de Souza[84], A. de Torres[74], J. Debosscher[36], E. del Pozo[44], M. Delbo[17], A. Delgado[3], H. E. Delgado[60], S. Diakite[58], C. Diener[3], E. Distefano[49], C. Dolding[24], P. Drazinos[85], J. Durán[57], B. Edvardsson[46], H. Enke[86], K. Eriksson[46], P. Esquej[87], G. Eynard Bontemps[18], C. Fabre[88], M. Fabrizio[53,54], S. Faigler[89], A. J. Falcão[90], M. Farràs Casas[5], L. Federici[26], G. Fedorets[55], P. Fernique[42], F. Figueras[5], F. Filippi[28], K. Findeisen[2], A. Fonti[28], E. Fraile[87], M. Fraser[3,91], B. Frézouls[18], M. Gai[25], S. Galleti[26], D. Garabato[51], F. García-Sedano[60], A. Garofalo[92,26], N. Garralda[5], A. Gavel[46], P. Gavras[2,32,85], J. Gerssen[86], R. Geyer[14], P. Giacobbe[25], G. Gilmore[3], S. Girona[93], G. Giuffrida[54,53], F. Glass[12], M. Gomes[47], M. Granvik[55,94], A. Gueguen[2,95], A. Guerrier[62], J. Guiraud[18], R. Gutiérrez-Sánchez[22], R. Haigron[2], D. Hatzidimitriou[85,32], M. Hauser[11,10], M. Haywood[2], U. Heiter[46], A. Helmi[75], J. Heu[2], T. Hilger[14], D. Hobbs[16], W. Hofmann[11], G. Holland[3], H. E. Huckle[24], A. Hypki[8,96], V. Icardi[28], K. Janßen[86], G. Jevardat de Fombelle[29], P. G. Jonker[77,63], Á. L. Juhász[97,98], F. Julbe[5], A. Karampelas[85,99], A. Kewley[3],

★ The full Table A.1 is only available at the CDS via anonymous ftp to cdsarc.u-strasbg.fr (130.79.128.5) or via http://cdsarc.u-strasbg.fr/viz-bin/qcat?J/A+A/616/A10

★★ Corresponding author: C. Babusiaux, e-mail: carine.babusiaux@univ-grenoble-alpes.fr

J. Klar[86], A. Kochoska[100,101], R. Kohley[15], K. Kolenberg[73,102,36], M. Kontizas[85], E. Kontizas[32], S. E. Koposov[3,103], G. Kordopatis[17], Z. Kostrzewa-Rutkowska[77,63], P. Koubsky[104], S. Lambert[31], A. F. Lanza[49], Y. Lasne[62], J.-B. Lavigne[62], Y. Le Fustec[105], C. Le Poncin-Lafitte[31], Y. Lebreton[2,106], S. Leccia[83], N. Leclerc[2], I. Lecoeur-Taibi[29], H. Lenhardt[11], F. Leroux[62], S. Liao[25,107,108], E. Licata[72], H. E. P. Lindstrøm[109,110], T. A. Lister[111], E. Livanou[85], A. Lobel[34], M. López[69], S. Managau[62], R. G. Mann[35], G. Mantelet[11], O. Marchal[2], J. M. Marchant[112], M. Marconi[83], S. Marinoni[53,54], G. Marschalkó[97,113], D. J. Marshall[114], M. Martino[28], G. Marton[97], N. Mary[62], D. Massari[75], G. Matijevič[86], T. Mazeh[89], P. J. McMillan[16], S. Messina[49], D. Michalik[16], N. R. Millar[3], D. Molina[5], R. Molinaro[83], L. Molnár[97], P. Montegriffo[26], R. Mor[5], R. Morbidelli[25], T. Morel[37], D. Morris[35], A. F. Mulone[28], T. Muraveva[26], I. Musella[83], G. Nelemans[63,36], L. Nicastro[26], L. Noval[62], W. O'Mullane[15,41], C. Ordénovic[17], D. Ordóñez-Blanco [29], P. Osborne[3], C. Pagani[4], I. Pagano[49], F. Pailler[18], H. Palacin[62], L. Palaversa[3,12], A. Panahi[89], M. Pawlak[115,116], A. M. Piersimoni[82], F.-X. Pineau[42], E. Plachy[97], G. Plum[2], E. Poggio[68,25], E. Poujoulet[117], A. Prša[101], L. Pulone[53], E. Racero[27], S. Ragaini[26], N. Rambaux[33], M. Ramos-Lerate[118], S. Regibo[36], C. Reylé[58], F. Riclet[18], V. Ripepi[83], A. Riva[25], A. Rivard[62], G. Rixon[3], T. Roegiers[119], M. Roelens[12], M. Romero-Gómez[5], N. Rowell[35], F. Royer[2], L. Ruiz-Dern[2], G. Sadowski[19], T. Sagristà Sellés[11], J. Sahlmann[15,120], J. Salgado[121], E. Salguero[38], N. Sanna[21], T. Santana-Ros[96], M. Sarasso[25], H. Savietto[122], M. Schultheis[17], E. Sciacca[49], M. Segol[123], J. C. Segovia[27], D. Ségransan[12], I-C. Shih[2], L. Siltala[55,124], A. F. Silva[47], R. L. Smart[25], K. W. Smith[10], E. Solano[69,125], F. Solitro[28], R. Sordo[6], S. Soria Nieto[5], J. Souchay[31], A. Spagna[25], F. Spoto[17,33], U. Stampa[11], I. A. Steele[112], H. Steidelmüller[14], C. A. Stephenson[22], H. Stoev[126], F. F. Suess[3], J. Surdej[37], L. Szabados[97], E. Szegedi-Elek[97], D. Tapiador[127,128], F. Taris[31], G. Tauran[62], M. B. Taylor[129], R. Teixeira[84], D. Terrett[59], P. Teyssandier[31], W. Thuillot[33], A. Titarenko[17], F. Torra Clotet[130], C. Turon[2], A. Ulla[131], E. Utrilla[44], S. Uzzi[28], M. Vaillant[62], G. Valentini[82], V. Valette[18], A. van Elteren[8], E. Van Hemelryck[34], M. Vaschetto[28], A. Vecchiato[25], J. Veljanoski[75], Y. Viala[2], D. Vicente[93], S. Vogt[119], C. von Essen[132], H. Voss[5], V. Votruba[104], S. Voutsinas[35], G. Walmsley[18], M. Weiler[5], O. Wertz[133], T. Wevers[3,63], Ł. Wyrzykowski[3,115], A. Yoldas[3], M. Žerjal[100,134], H. Ziaeepour[58], J. Zorec[135], S. Zschocke[14], S. Zucker[136], C. Zurbach[45], and T. Zwitter[100]

(Affiliations can be found after the references)

Received 16 February 2018 / Accepted 16 April 2018

ABSTRACT

Context. *Gaia* Data Release 2 provides high-precision astrometry and three-band photometry for about 1.3 billion sources over the full sky. The precision, accuracy, and homogeneity of both astrometry and photometry are unprecedented.

Aims. We highlight the power of the *Gaia* DR2 in studying many fine structures of the Hertzsprung-Russell diagram (HRD). *Gaia* allows us to present many different HRDs, depending in particular on stellar population selections. We do not aim here for completeness in terms of types of stars or stellar evolutionary aspects. Instead, we have chosen several illustrative examples.

Methods. We describe some of the selections that can be made in *Gaia* DR2 to highlight the main structures of the *Gaia* HRDs. We select both field and cluster (open and globular) stars, compare the observations with previous classifications and with stellar evolutionary tracks, and we present variations of the *Gaia* HRD with age, metallicity, and kinematics. Late stages of stellar evolution such as hot subdwarfs, post-AGB stars, planetary nebulae, and white dwarfs are also analysed, as well as low-mass brown dwarf objects.

Results. The *Gaia* HRDs are unprecedented in both precision and coverage of the various Milky Way stellar populations and stellar evolutionary phases. Many fine structures of the HRDs are presented. The clear split of the white dwarf sequence into hydrogen and helium white dwarfs is presented for the first time in an HRD. The relation between kinematics and the HRD is nicely illustrated. Two different populations in a classical kinematic selection of the halo are unambiguously identified in the HRD. Membership and mean parameters for a selected list of open clusters are provided. They allow drawing very detailed cluster sequences, highlighting fine structures, and providing extremely precise empirical isochrones that will lead to more insight in stellar physics.

Conclusions. *Gaia* DR2 demonstrates the potential of combining precise astrometry and photometry for large samples for studies in stellar evolution and stellar population and opens an entire new area for HRD-based studies.

Key words. parallaxes – Hertzsprung-Russell and C-M diagrams – solar neighborhood – stars: evolution

1. Introduction

The Hertzsprung-Russell diagram (HRD) is one of the most important tools in stellar studies. It illustrates empirically the relationship between stellar spectral type (or temperature or colour index) and luminosity (or absolute magnitude). The position of a star in the HRD is mainly given by its initial mass, chemical composition, and age, but effects such as rotation, stellar wind, magnetic field, detailed chemical abundance, overshooting, and non-local thermal equilibrium also play a role. Therefore, the detailed HRD features are important to constrain stellar structure and evolutionary studies as well as stellar atmosphere modelling. Up to now, a proper understanding of the physical process in the stellar interior and the exact contribution of each of the effects mentioned are missing because we lack large precise and homogeneous samples that cover the full

HRD. Moreover, a precise HRD provides a great framework for exploring stellar populations and stellar systems.

Up to now, the most complete solar neighbourhood empirical HRD could be obtained by combining the HIPPARCOS data (Perryman et al. 1995) with nearby stellar catalogues to provide the faint end (e.g. Gliese & Jahreiß 1991; Henry & Jao 2015). Clusters provide empirical HRDs for a range of ages and metal contents and are therefore widely used in stellar evolution studies. To be conclusive, they need homogeneous photometry for inter-comparisons and astrometry for good memberships.

With its global census of the whole sky, homogeneous astrometry, and photometry of unprecedented accuracy, *Gaia* DR2 is setting a new major step in stellar, galactic, and extragalactic studies. It provides position, trigonometric parallax, and proper motion as well as three broad-band magnitudes (G, $G_{\rm BP}$, and $G_{\rm RP}$) for more than a billion objects brighter than $G \sim 20$, plus radial velocity for sources brighter than $G_{\rm RVS} \sim 12$ mag and photometry for variable stars (Gaia Collaboration 2018a). The amount, exquisite quality, and homogeneity of the data allows reaching a level of detail in the HRDs that has never been reached before. The number of open clusters with accurate parallax information is unprecedented, and new open clusters or associations will be discovered. *Gaia* DR2 provides absolute parallax for faint red dwarfs and the faintest white dwarfs for the first time.

This paper is one of the papers accompanying the *Gaia* DR2 release. The following papers describe the data used here: Gaia Collaboration (2018a) for an overview, Lindegren et al. (2018) for the astrometry, Evans et al. (2018) for the photometry, and Arenou et al. (2018) for the global validation. Someone interested in this HRD paper may also be interested in the variability in the HRD described in Gaia Collaboration (2018b), in the first attempt to derive an HRD using temperatures and luminosities from the *Gaia* DR2 data of Andrae et al. (2018), in the kinematics of the globular clusters discussed in Gaia Collaboration (2018c), and in the field kinematics presented in Gaia Collaboration (2018d).

In this paper, Sect. 2 presents a global description of how we built the *Gaia* HRDs of both field and cluster stars, the filters that we applied, and the handling of the extinction. In Sect. 3 we present our selection of cluster data; the handling of the globular clusters is detailed in Gaia Collaboration (2018c) and the handling of the open clusters is detailed in Appendix A. Section 4 discusses the main structures of the *Gaia* DR2 HRD. The level of the details of the white dwarf sequence is so new that it leads to a more intense discussion, which we present in a separate Sect. 5. In Sect. 6 we compare clusters with a set of isochrones. In Sect. 7 we study the variation of the *Gaia* HRDs with kinematics. We finally conclude in Sect. 8.

2. Building the *Gaia* HRDs

This paper presents the power of the *Gaia* DR2 astrometry and photometry in studying fine structures of the HRD. For this, we selected the most precise data, without trying to reach completeness. In practice, this means selecting the most precise parallax and photometry, but also handling the extinction rigorously. This can no longer be neglected with the depth of the *Gaia* precise data in this release.

2.1. Data filtering

The *Gaia* DR2 is unprecedented in both the quality and the quantity of its astrometric and photometric data. Still, this is an intermediate data release without a full implementation of the complexity of the processing for an optimal usage of the data. A detailed description of the astrometric and photometric features is given in Lindegren et al. (2018) and Evans et al. (2018), respectively, and Arenou et al. (2018) provides a global validation of them. Here we highlight the features that are important to be taken into account in building *Gaia* DR2 HRDs and present the filters we applied in this paper.

Concerning the astrometric content (Lindegren et al. 2018), the median uncertainty for the bright source ($G < 14$ mag) parallax is 0.03 mas. The systematics are lower than 0.1 mas, and the parallax zeropoint error is about 0.03 mas. Significant correlations at small spatial scale between the astrometric parameters are also observed. Concerning the photometric content (Evans et al. 2018), the precision at $G = 12$ is around 1 mmag in the three passbands, with systematics at the level of 10 mmag.

Lindegren et al. (2018) described that a five-parameter solution is accepted only if at least six visibility periods are used (e.g. the number of groups of observations separated from other groups by a gap of at least four days, the parameter is named `visibility_periods_used` in the *Gaia* archive). The observations need to be well spread out in time to provide reliable five-parameter solutions. Here we applied a stronger filter on this parameter: `visibility_periods_used>8`. This removes strong outliers, in particular at the faint end of the local HRD (Arenou et al. 2018). It also leads to more incompleteness, but this is not an issue for this paper.

The astrometric excess noise is the extra noise that must be postulated to explain the scatter of residuals in the astrometric solution. When it is high, it either means that the astrometric solution has failed and/or that the studied object is in a multiple system for which the single-star solution is not reliable. Without filtering on the astrometric excess noise, artefacts are present in particular between the white dwarf and the main sequence in the *Gaia* HRDs. Some of those stars are genuine binaries, but the majority are artefacts (Arenou et al. 2018). To still see the imprint of genuine binaries on the HRD while removing most of the artefacts, we adopted the filter proposed in Appendix C of Lindegren et al. (2018): $\sqrt{\chi^2/(\nu'-5)} < 1.2\max(1, \exp(-0.2(G-19.5))$ with χ^2 and ν' given as `astrometric_chi2_al` and `astrometric_n_good_obs_al`, respectively, in the *Gaia* archive. A similar clean-up of the HRD is obtained by the `astrometric_excess_noise<1` criterion, but this is less optimised for the bright stars because of the degrees of freedom (DOF) issue (Lindegren et al. 2018, Appendix A).

We built the *Gaia* HRDs by simply estimating the absolute *Gaia* magnitude in the G band for individual stars using $M_G = G + 5 + 5\log_{10}(\varpi/1000)$, with ϖ the parallax in milliarcseconds (plus the extinction, see next section). This is valid only when the relative precision on the parallax is lower than about 20% (Luri et al. 2018). We aim here to examine the fine structures in the HRD revealed by *Gaia* and therefore adopt a 10% relative precision criterion, which corresponds to an uncertainty on M_G smaller than 0.22 mag: `parallax_over_error>10`.

Similarly, we apply filters on the relative flux error on the G, $G_{\rm BP}$, and $G_{\rm RP}$ photometry: `phot_g_mean_flux_over_error>50` ($\sigma_G < 0.022$ mag), `phot_rp_mean_flux_over_error>20`, and `phot_bp_mean_flux_over_error>20` ($\sigma_{G_{\rm XP}} < 0.054$ mag). These criteria may remove variable stars, which are specifically studied in Gaia Collaboration (2018b).

The processing of the photometric data in DR2 has not treated blends in the windows of the blue and red photometers (BP and RP). As a consequence, the measured BP and RP fluxes may include the contribution of flux from nearby sources, the highest impact being in sky areas of high stellar density, such as

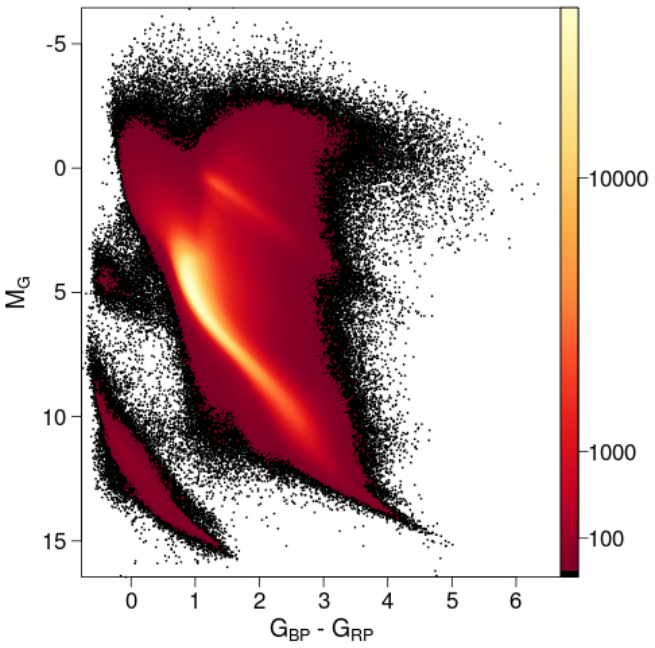

Fig. 1. Full *Gaia* colour-magnitude diagram of sources with the filters described in Sect. 2.1 applied (65 921 112 stars). The colour scale represents the square root of the relative density of stars.

the inner regions of globular clusters, the Magellanic Clouds, or the Galactic Bulge. During the validation process, misdeterminations of the local background have also been identified. In some cases, this background is due to nearby bright sources with long wings of the point spread function that have not been properly subtracted. In other cases, the background has a solar type spectrum, which indicates that the modelling of the background flux is not good enough. The faint sources are most strongly affected. For details, see Evans et al. (2018) and Arenou et al. (2018). Here, we have limited our analysis to the sources within the empirically defined locus of the $(I_{BP} + I_{RP})/I_G$ fluxes ratio as a function of $G_{BP} - G_{RP}$ colour: `phot_bp_rp_excess_factor`$> 1.0 + 0.015\ (G_{BP} - G_{RP})^2$ and `phot_bp_rp_excess_factor`$< 1.3 + 0.06\ (G_{BP} - G_{RP})^2$. The *Gaia* archive query combining all the filters presented here is provided in Appendix B.

2.2. Extinction

The dust that is present along the line of sight towards the stars leads to a dimming and reddening of their observed light. In the full colour – absolute magnitude diagram presented in Fig. 1, the effect of the extinction is particularly striking for the red clump. The de-reddened HRD using the extinction provided together with DR2 is presented in Andrae et al. (2018). To study the fine structures of the *Gaia* HRD for field stars, we selected here only low-extinction stars. High galactic latitude and close-by stars located within the local bubble (the reddening is almost negligible within ~60 pc of the Sun Lallement et al. 2003) are affected less from the extinction, and we did not apply further selection for them. To select low-extinction stars away from these simple cases, we followed Ruiz-Dern et al. (2018) and used the 3D extinction map of Capitanio et al. (2017)[1], which is particularly well adapted to finding holes in the interstellar medium and to select field stars with $E(B - V) < 0.015$.

[1] http://stilism.obspm.fr/

For globular clusters we used literature extinction values (Sect. 3.3), while for open clusters, they are derived together with the ages (Sect. 3.2). Detailed comparisons of these global cluster extinctions with those that can be derived from the extinctions provided by *Gaia* DR2 can be found in Arenou et al. (2018). To transform the global cluster extinction easily into the *Gaia* passbands while taking into account the extinction coefficients dependency on colour and extinction itself in these large passbands (e.g. Jordi et al. 2010), we used the same formulae as Danielski et al. (2018) to compute the extinction coefficients $k_X = A_X/A_0$:

$$k_X = c_1 + c_2(G_{BP} - G_{RP})_0 + c_3(G_{BP} - G_{RP})_0^2 + c_4(G_{BP} - G_{RP})_0^3 + c_5 A_0 + c_6 A_0^2 + c_7(G_{BP} - G_{RP})_0 A_0. \quad (1)$$

As in Danielski et al. (2018), this formula was fitted on a grid of extinctions convolving the latest *Gaia* passbands presented in Evans et al. (2018) with Kurucz spectra (Castelli & Kurucz 2003) and the Fitzpatrick & Massa (2007) extinction law for 3500 K $< T_{\rm eff} <$10 000 K by steps of 250 K, $0.01 < A_0 < 5$ mag by steps of 0.01 mag and two surfaces gravities: $\log g = 2.5$ and 4. The resulting coefficients are provided in Table 1. We assume in the following $A_0 = 3.1\,E(B - V)$.

Some clusters show high differential extinction across their field, which broadens their colour-magnitude diagrams. These clusters have been discarded from this analysis.

3. Cluster data

Star clusters can provide observational isochrones for a range of ages and chemical compositions. Most suitable are clusters with low and uniform reddening values and whose magnitude range is wide, which would limit our sample to the nearest clusters. Such a sample would, however, present a rather limited range in age and chemical composition.

3.1. Membership and astrometric solutions

Two types of astrometric solutions were applied. The first type is applicable to nearby clusters. For the second *Gaia* data release, the nearby "limit" was set at 250 pc. Within this limit, the parallax and proper motion data for the individual cluster members are sufficiently accurate to reflect the effects of projection along the line of sight, thus enabling the 3D reconstruction of the cluster. This is further described in Appendix A.1.

For these nearby clusters, the size of the cluster relative to its distance will contribute a significant level of scatter to the HRD if parallaxes for individual cluster members are not taken into account. With a relative accuracy of about 1% in the parallax measurement, an error contribution of around 0.02 in the absolute magnitude is possible. For a large portion of the *Gaia* photometry, the uncertainties are about 5–10 times lower, making the parallax measurement still the main contributor to the uncertainty in the absolute magnitude. The range of differences in parallax between the cluster centre and an individual cluster member depends on the ratio of the cluster radius over the cluster distance. At a radius of 15 pc, the 1% level is found for a cluster at 1.5 kpc, or a parallax of 0.67 mas. In *Gaia* DR2, formal uncertainties on the parallaxes may reach levels of just lower than 10 μas, but the overall uncertainty from localised systematics is about 0.025 mas. If this value is considered the 1% uncertainty level, then a resolution of a cluster along the line of sight, using *Gaia* DR2, becomes possible for clusters within 400 pc, and realistic for clusters within about 250 pc.

Table 1. Parameters used to derive the *Gaia* extinction coefficients as a function of colour and extinction (Eq. (1)).

	c_1	c_2	c_3	c_4	c_5	c_6	c_7
k_G	0.9761	−0.1704	0.0086	0.0011	−0.0438	0.0013	0.0099
k_{BP}	1.1517	−0.0871	−0.0333	0.0173	−0.0230	0.0006	0.0043
k_{RP}	0.6104	−0.0170	−0.0026	−0.0017	−0.0078	0.00005	0.0006

For clusters at larger distances, the mean cluster proper motion and parallax are derived directly from the observed astrometric parameters for the individual cluster members. The details of this procedure are presented in Appendix A.2.

3.2. Selection of open clusters

Our sample of open clusters consists of the mostly well-defined and fairly rich clusters within 250 pc, and a selection of mainly rich clusters at larger distances, covering a wider range of ages, mostly up to 1.5 kpc, with a few additional clusters at larger distances where these might supply additional information at more extreme ages. For very young clusters, the definition of the cluster is not always clear, as the youngest systems are mostly found embedded in OB associations, producing large samples of similar proper motions and parallaxes. Very few clusters appear to survive to an "old age", but those that do are generally rich, allowing good membership determination. The final selection consists of 9 clusters within 250 pc, and 37 clusters up to 5.3 kpc. Of the latter group, only 23 were finally used for construction of the colour-magnitude diagram; these clusters are listed together with the 9 nearby clusters in Table 2. For the remaining 14 clusters, the colour-magnitude diagrams appeared to be too much affected by interstellar reddening variations. More details on the astrometric solutions are provided in Appendix A; the solutions are presented for the nearby clusters in Table A.3 and for the more distant clusters in Table A.4. Figure 2 shows the combined HRD of these clusters, coloured according to their ages as provided in Table 2. The main-sequence turn-off and red clump evolution with age is clearly visible. The age difference is also shown for lower mass stars, the youngest stars lie slightly above the main sequence of the others. The white dwarf sequence is also visible.

3.3. Selection of globular clusters

The details of selecting globular clusters are presented in Gaia Collaboration (2018c). A major issue for the globular cluster data is the uncertainties on the parallaxes that result from the systematics, which is in most cases about one order of magnitude larger than the standard uncertainties on the mean parallax determinations for the globular clusters. The implication of this is that the parallaxes as determined with the *Gaia* data cannot be used to derive the distance moduli needed to prepare the composite HRD for the globular clusters. Instead, we had to rely on distances as quoted in the literature, for which we used the tables (2010 edition) provided online by Harris (1996). The inevitable drawback is that these distances and reddening values have been obtained through isochrone fitting, and the application of these values to the *Gaia* data will provide only limited new information. The main advantage is the possibility of comparing the HRDs of all globular clusters within a single, accurate photometric system. The combined HRD for 14 globular clusters is shown in Fig. 3, the summary data for these clusters is presented in Table 3. The photometric data originate predominantly from the outskirts of the clusters, as in the cluster centres the crowding often affects the colour index determination. Figure 3 shows the blue horizontal branch populated with the metal-poor clusters and the move of the giant branch towards the blue with decreasing metallicity.

An interesting comparison can be made between the most metal-rich well-populated globular cluster of our sample, 47 Tuc (NGC 104), and one of the oldest open clusters, M67 (NGC 2682) (Fig. 4). This provides the closest comparison between the HRDs of an open and a globular cluster. Most open clusters are much younger, while most globular clusters are much less metal rich.

Table 2. Overview of reference values used in constructing the composite HRD for open clusters (Fig. 2).

Cluster	DM	log(age)	[Fe/H]	$E(B-V)$	Memb
Hyades	3.389	8.90	0.13	0.001	480
Coma Ber	4.669	8.81	0.00	0.000	127
Pleiades	5.667	8.04	−0.01	0.045	1059
IC 2391	5.908	7.70	−0.01	0.030	254
IC 2602	5.914	7.60	−0.02	0.031	391
α Per	6.214	7.85	0.14	0.090	598
Praesepe	6.350	8.85	0.16	0.027	771
NGC 2451A	6.433	7.78	−0.08	0.000	311
Blanco 1	6.876	8.06	0.03	0.010	361
NGC 6475	7.234	8.54	0.02	0.049	874
NGC 7092	7.390	8.54	0.00	0.010	248
NGC 6774	7.455	9.30	0.16	0.080	165
NGC 2232	7.575	7.70	0.11	0.031	241
NGC 2547	7.980	7.60	−0.14	0.040	404
NGC 2516	8.091	8.48	0.05	0.071	1727
Trumpler 10	8.223	7.78	−0.12	0.056	407
NGC 752	8.264	9.15	−0.03	0.040	259
NGC 6405	8.320	7.90	0.07	0.139	544
IC 4756	8.401	8.98	0.02	0.128	515
NGC 3532	8.430	8.60	0.00	0.022	1802
NGC 2422	8.436	8.11	0.09	0.090	572
NGC 1039	8.552	8.40	0.02	0.077	497
NGC 6281	8.638	8.48	0.06	0.130	534
NGC 6793	8.894	8.78		0.272	271
NGC 2548	9.451	8.74	0.08	0.020	374
NGC 6025	9.513	8.18		0.170	431
NGC 2682	9.726	9.54	0.03	0.037	1194
IC 4651	9.889	9.30	0.12	0.040	932
NGC 2323	10.010	8.30		0.105	372
NGC 2447	10.088	8.74	−0.05	0.034	681
NGC 2360	10.229	8.98	−0.03	0.090	848
NGC 188	11.490	9.74	0.11	0.085	956

Notes. Distance moduli (DM) as derived from the *Gaia* astrometry; ages and reddening values as derived from *Gaia* photometry (see Sect. 6), with distances fixed on astrometric determinations; metallicities from Netopil et al. (2016); Memb: the number of members with *Gaia* photometric data after application of the photometric filters.

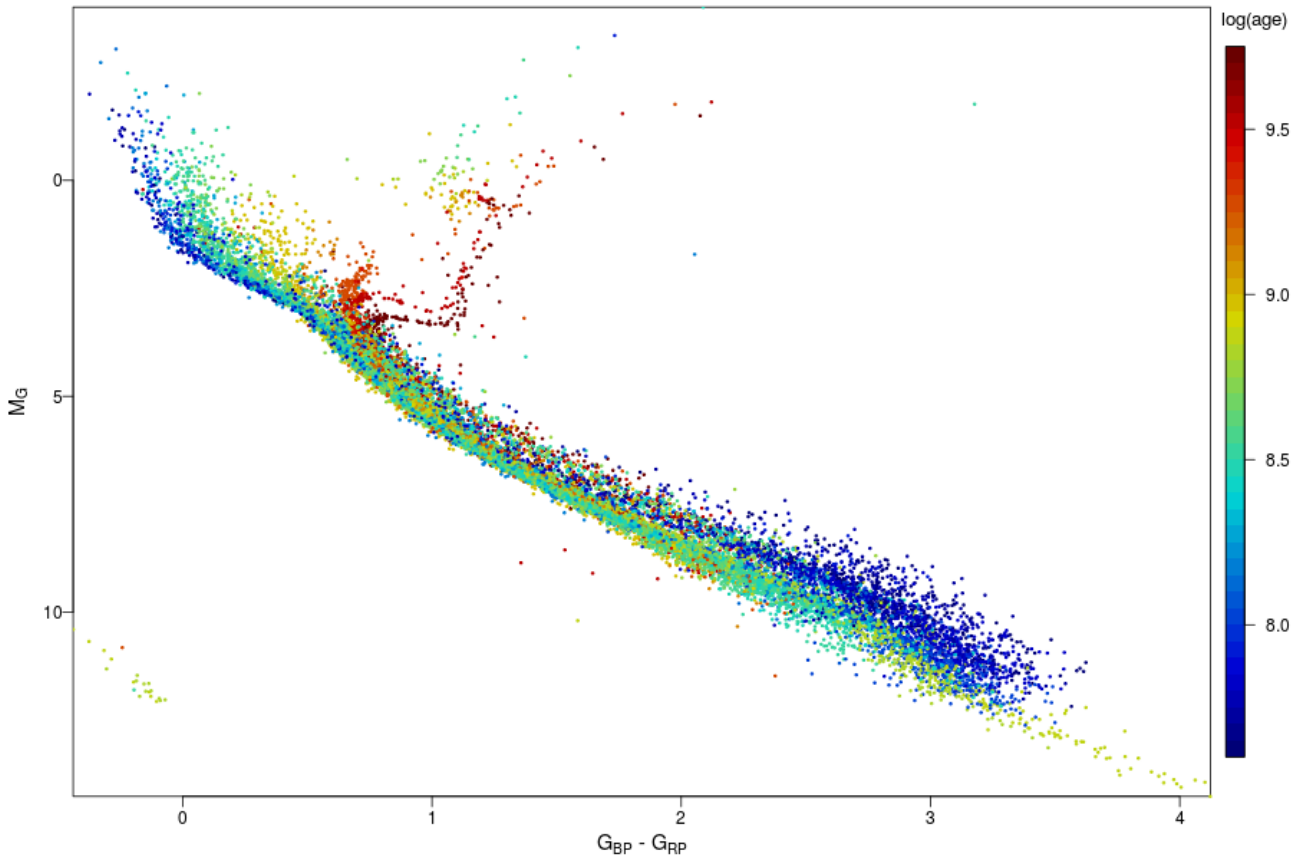

Fig. 2. Composite HRD for 32 open clusters, coloured according to log(age), using the extinction and distance moduli as determined from the *Gaia* data (Table 2).

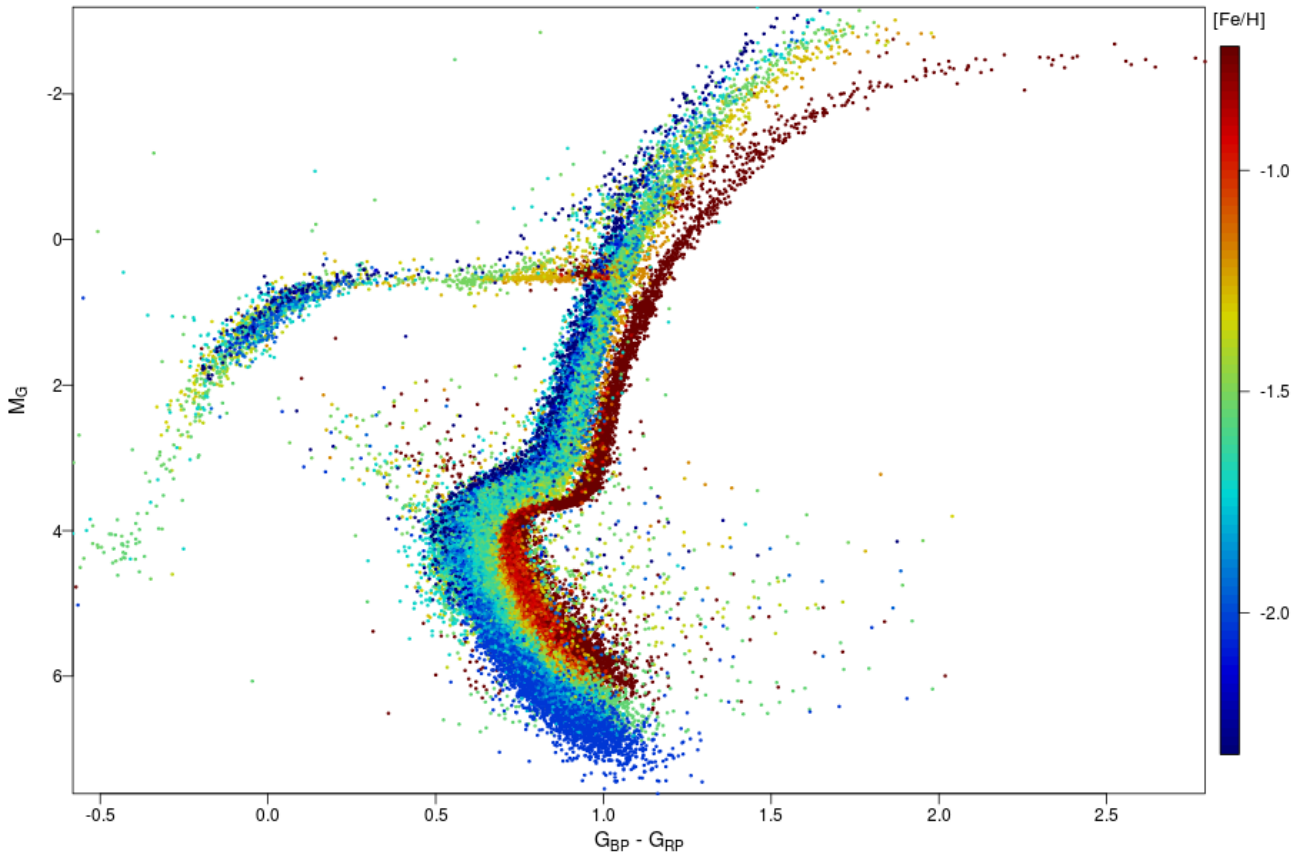

Fig. 3. Composite HRD for 14 globular clusters, coloured according to metallicity (Table 3).

Table 3. Reference data for 14 globular clusters used in the construction of the combined HRD (Fig. 3).

NGC	DM	Age (Gyr)	[Fe/H]	$E(B-V)$	Memb
104	13.266	12.75[a]	−0.72	0.04	21580
288	14.747	12.50[a]	−1.31	0.03	1953
362	14.672	11.50[a]	−1.26	0.05	1737
1851	15.414	13.30[c]	−1.18	0.02	744
5272	15.043	12.60[b]	−1.50	0.01	9086
5904	14.375	12.25[a]	−1.29	0.03	3476
6205	14.256	13.00[a]	−1.53	0.02	10311
6218	13.406	13.25[a]	−1.37	0.19	3127
6341	14.595	13.25[a]	−2.31	0.02	1432
6397	11.920	13.50[a]	−2.02	0.18	10055
6656	12.526	12.86[c]	−1.70	0.35	9542
6752	13.010	12.50[a]	−1.54	0.04	10779
6809	13.662	13.50[a]	−1.94	0.08	8073
7099	14.542	13.25[a]	−2.27	0.03	1016

Notes. Data on distance moduli (DM), [Fe/H] and $E(B–V)$ from Harris (1996), 2010 edition, [(a)] Dotter et al. (2010), [(b)] Denissenkov et al. (2017), [(c)] Powalka et al. (2017) for age estimates. Memb: cluster members with photometry after application of photometric filters.

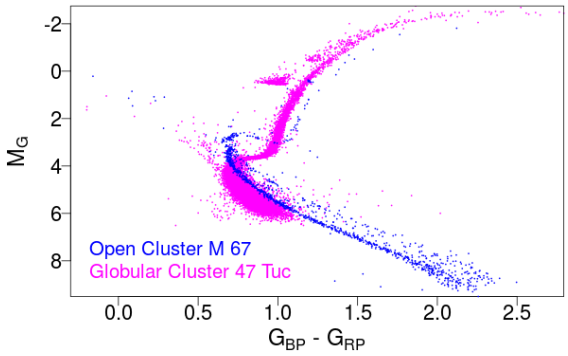

Fig. 4. Comparison between the HRDs of 47 Tuc (NGC 104, Age = 12.75 Gyr, [Fe/H] = −0.72), one of the most metal-rich globular clusters (magenta dots), and M 67 (NGC 2682, Age = 3.47 Gyr, [Fe/H] = 0.03), one of the oldest open clusters (blue dots).

4. Details of the *Gaia* HRDs

In the following, several field star HRDs are presented. Unless otherwise stated, the filters presented in Sect. 2.1, including the $E(B-V) < 0.015$ mag criteria, were applied. The HRDs use a red colour scale that represents the square root of the density of stars. The *Gaia* DR2 HRD of the low-extinction stars is represented in Fig. 5. The approximate equivalent temperature and luminosity to the $G_{BP} - G_{RP}$ colour and the absolute *Gaia* M_G magnitude provided in the figure were determined using the PARSEC isochrones (Marigo et al. 2017) for main-sequence stars.

Figure 6 shows the local *Gaia* HRDs using several cuts in parallax, still with the filters of Sect. 2.1, but without the need to apply the $E(B-V) < 0.015$ mag extinction criteria, as these sources mostly lie within the local bubble.

4.1. Main sequence

The main sequence is very thin, both in fields and in clusters. This is very clearly visible in Fig. 7, which shows the HRDs of

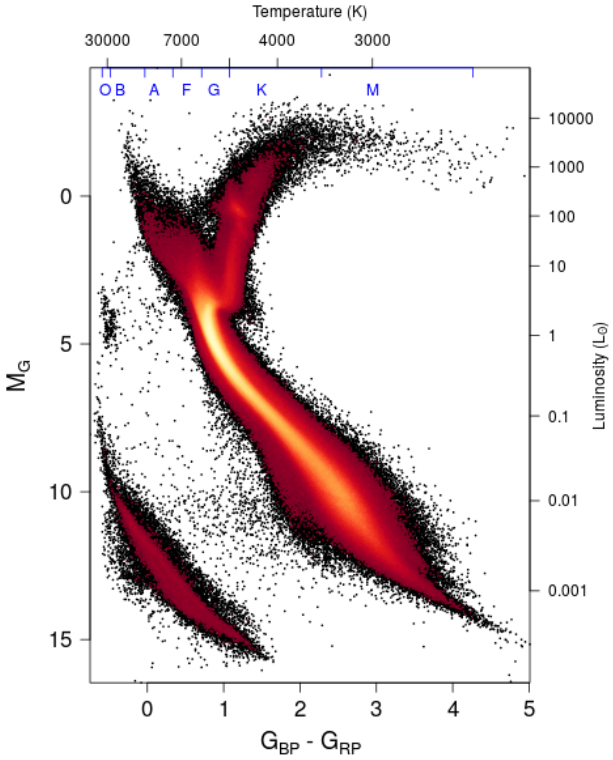

Fig. 5. *Gaia* HRD of sources with low extinction ($E(B–V) <$ 0.015 mag) satisfying the filters described in Sect. 2.1 (4 276 690 stars). The colour scale represents the square root of the density of stars. Approximate temperature and luminosity equivalents for main-sequence stars are provided at the top and right axis, respectively, to guide the eye.

the Hyades and Praesepe clusters (ages ∼700 Myr), which accurately overlap, as has previously been noticed in van Leeuwen (2009) and confirmed in Gaia Collaboration (2017). This figure shows the very narrow sequence described by the stars in both clusters, as well as the scattering of double stars up to 0.75 magnitudes above the main sequence. The remaining width of the main sequence is still largely explained as due to the uncertainties in the parallax of the individual stars, and the underlying main sequence is likely to be even narrower.

The binary sequence spread is visible throughout the main sequence (Figs. 5 and 6), and most clearly in open clusters (Fig. 7, see also Sect. 6). It is most preeminent for field stars below $M_G = 13$. Figure 8 shows the main-sequence fiducial of the local HRD shifted by 0.753 mag, which corresponds to two identical stars in an unresolved binary system observed with the same colour but twice the luminosity of the equivalent single star. See Hurley & Tout (1998), for instance, for a discussion of this strong sequence. Binaries with a main-sequence primary and a giant companion would lie much higher in the diagram, while binaries with a late-type main-sequence primary and a white dwarf companion lie between the white dwarf and the main sequence, as is shown in Fig. 5, for example.

The main sequence is thicker between $10 < M_G < 13$ (Figs. 2, 5 and 6). The youngest main-sequence stars lie on the upper part of the main sequence (in blue in Fig. 2). The subdwarfs, which are metal-poor stars associated with the halo, are visible in the lower part of the local HRD (in red in Fig. 2, see also Sect. 7).

The main-sequence turn-off variation with age is clearly illustrated in Fig. 2, and the variation with metallicity is shown

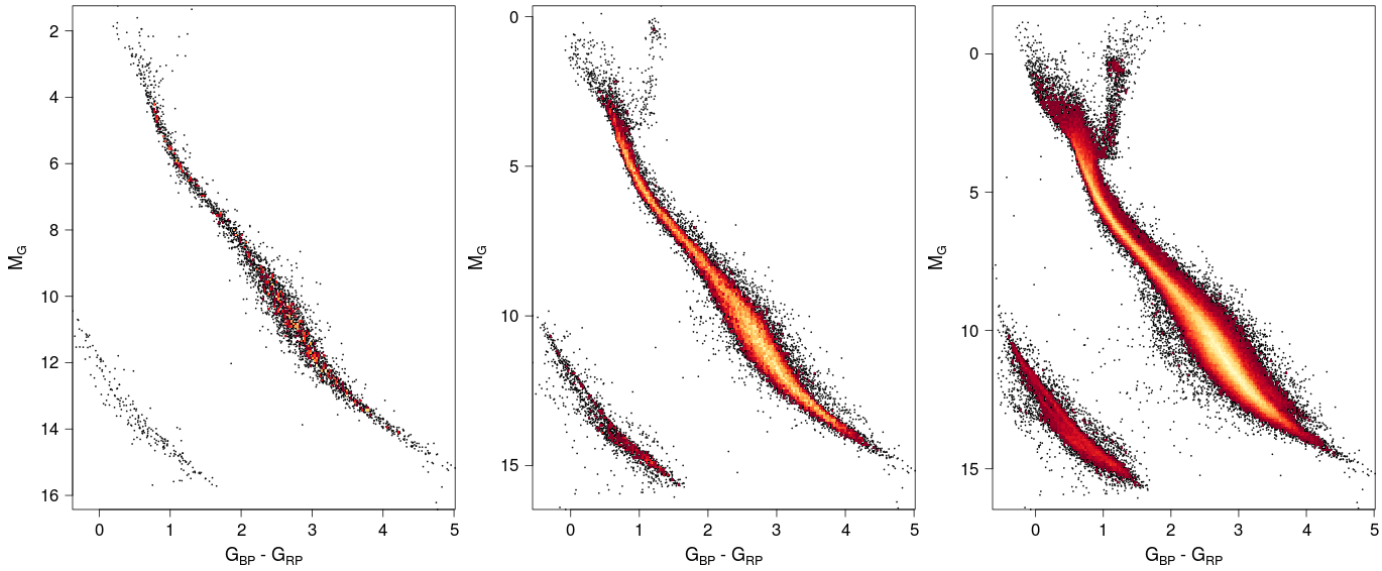

Fig. 6. Solar neighbourhood *Gaia* HRDs for *panel a*: $\varpi > 40$ mas (25 pc, 3724 stars), *panel b*: $\varpi > 20$ mas (50 pc, 29 683 stars), and *panel c*: $\varpi > 10$ mas (100 pc, 212 728 stars).

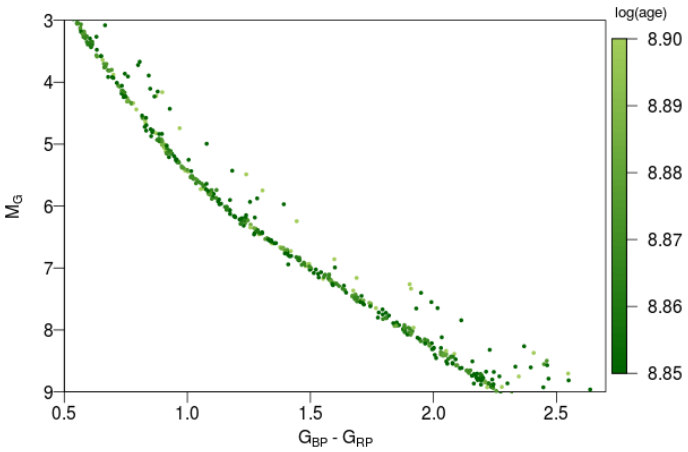

Fig. 7. Extract of the HRD for the Hyades and Praesepe clusters, showing the detailed agreement between the main sequences of the two clusters, the narrowness of the combined main sequence, and a scattering of double stars up to 0.75 mag above the main sequence.

in Fig. 3. Blue stragglers are also visible over the main-sequence turn-off (Fig. 4).

Between the main sequence and the subgiants lies a tail of stars around $M_G = 4$ and $G_{BP} - G_{RP} = 1.5$. These stars shows variability and may be associated with RS Canum Venaticorum variables, which are close binary stars (Gaia Collaboration 2018b).

4.2. Brown dwarfs

To study the location of the low-mass objects in the *Gaia* HRD, we used the *Gaia* ultracool dwarf sample (GUCDS) compiled by Smart et al. (2017). It includes 1886 brown dwarfs (BD) of L, T, and Y types, although a substantial fraction of them are too faint for *Gaia*. We note that the authors found 328 BDs in common with the *Gaia* DR1 catalogue (Gaia Collaboration 2016).

The crossmatch between the 2MASS catalogue (Skrutskie et al. 2006) and *Gaia* DR2 provided within the *Gaia* archive (Marrese et al. 2018) has been used to identify GUCDS entries. The resulting sample includes 601 BDs. Of these, 527 have

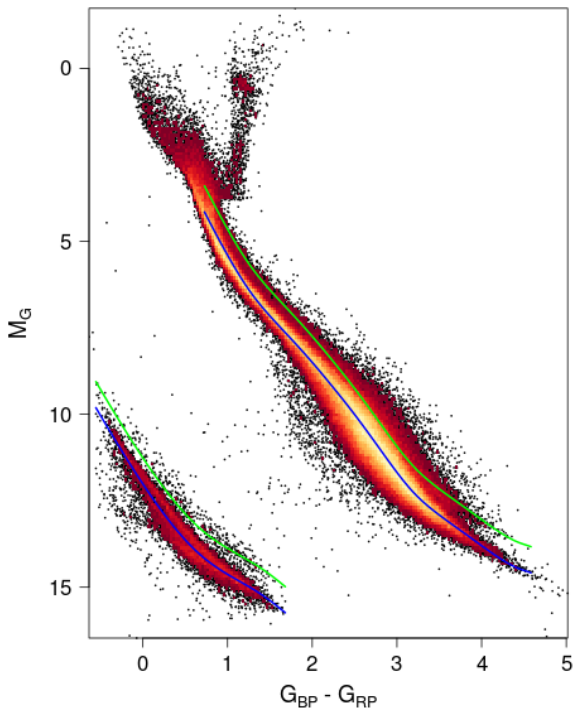

Fig. 8. Same as Fig. 6c, overlaid in blue with the median fiducial and in green with the same fiducial shifted by −0.753 mag, corresponding to an unresolved binary system of two identical stars.

five-parameter solutions (coordinates, proper motions, and parallax) and full photometry (G, G_{BP}, and G_{RP}). Most of these BDs have parallaxes higher than 4 mas (equivalent to 250 pc in distance) and relative parallax errors smaller than 25%. They also have astrometric excess noise larger than 1 mas and a high $(I_{BP} + I_{RP})/I_G$ flux ratio. They are faint red objects with very low flux in the BP wavelength range of their spectrum. Any background under-estimation causes the measured BP flux to increase to more than it should be, yielding high flux ratios, the highest ratios are derived for the faintest BDs. The filters presented in Sect. 2.1 therefore did not allow us to retain them.

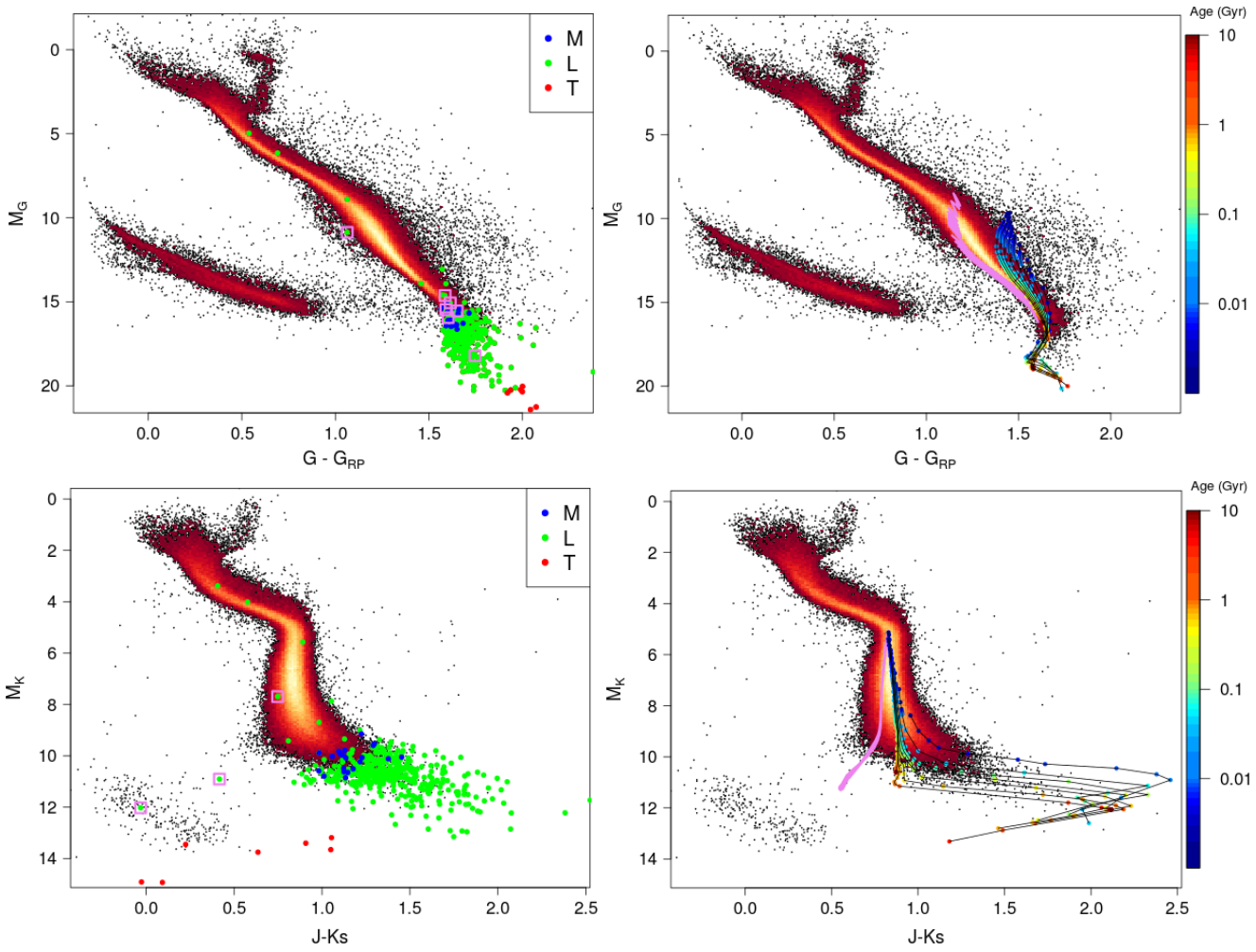

Fig. 9. *Panel a*: *Gaia* HRD of the stars with $\varpi > 10$ mas with adapted photometric filters (see text, 240 703 stars) overlaid with all cross-matched GUCDS (Smart et al. 2017) stars with $\sigma_\varpi/\varpi < 10\%$ in blue (M type), green (L type), and red (T type). Pink squares are added around stars with tangential velocity $V_T > 200\,\mathrm{km\,s^{-1}}$. *Panel b*: BT-Settl tracks (Baraffe et al. 2015) of solar metallicity for masses from 0.01 $M_\odot$ to 0.08 $M_\odot$ in steps of 0.01 (the upper tracks correspond to lower masses) plus in pink the same tracks for [M/H] = −1.0. *Panels c* and *d*: same diagrams using the 2MASS colours.

We accordingly adapted our filters for the background stars of Fig. 9. We plot the HRD using the $G - G_{RP}$ colour instead of $G_{BP} - G_{RP}$ because of the poor quality of G_{BP} for these faint red sources. We applied the same astrometric filters as for Fig. 6c, but we did not filter the fluxes ratio or the G_{BP} photometric uncertainties. More dispersion is present in this diagram than in Fig. 6c because of this missing filter, but the faint red sources we study here are represented better.

The 470 BDs for which DR2 provides parallaxes better than 10%, and the G and G_{RP} magnitudes are overlaid in Fig. 9 without any filtering. The sequence of BDs follows the sequence of low-mass stars. The absolute magnitudes of four stars are too bright, most probably because of a cross-match issue. In Fig. 9a the M-, L- and T-type BDs are sorted according to the classification in GUCDS. There are 21, 443, and 7 of each type, respectively. We also present in Fig. 9c the corresponding HRD using 2MASS colours with the 2MASS photometric quality flag AAA (applied to background and GUCDS stars). Figure 9b and 9d includes BT-Settl tracks[2] (Baraffe et al. 2015) for masses <0.08 $M_\odot$ that were computed using the nominal *Gaia* passbands. With the *Gaia* $G - G_{RP}$ colour, the sequence of M, L, T types is continuous and relatively thin. Conversely, the spread in the near-infrared is larger and the L/T transition feature is strongly seen with a shift of $J - K_s$ to the blue, which is due to a drastic change in the brown dwarf cloud properties (e.g. Saumon & Marley 2008). Some GUCDS L-type stars with very blue 2MASS colours seem at first sight intriguing, but their location might be consistent with metal-poor tracks (Fig. 9d). Following Faherty et al. (2009), we studied their kinematics, which are indeed consistent with the halo kinematic cut of the tangential velocity $V_T > 200\,\mathrm{km\,s^{-1}}$ (see Sect. 7). A kinematic selection of the global HRD as done in Sect. 7 but using the 2MASS colours confirms the blue tail of the bottom of the main sequence in the near-infrared for the halo kinematic selection.

[2] https://phoenix.ens-lyon.fr/Grids/BT-Settl/CIFIST2011bc

4.3. Giant branch

The clusters clearly illustrate the change in global shape of the giant branch with age and metallicity (Figs. 2 and 3). For field stars, there are fewer giants than dwarfs in the first 100 pc. To observe the field giant branch in more detail, we therefore extended our selection to 500 pc with the low-extinction selection ($E(B - V) < 0.015$, see Sect. 2.2) for Fig. 10.

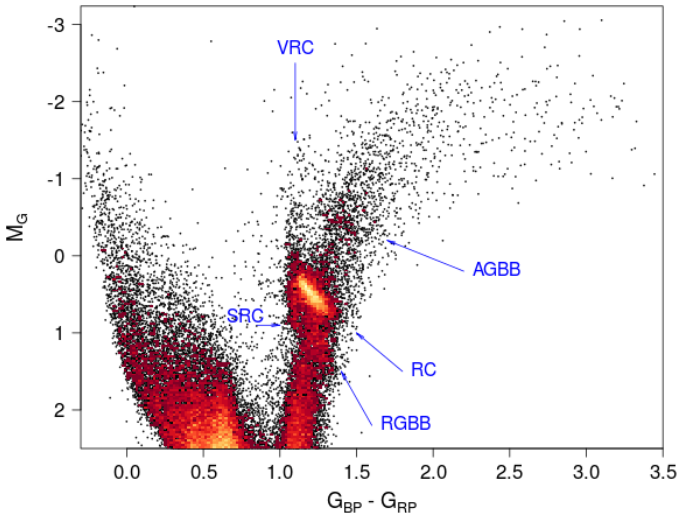

Fig. 10. *Gaia* HRD of low-extinction nearby giants: $\varpi > 2$ mas (500 pc), $E(B-V) < 0.015$ and $M_G < 2.5$ (29 288 stars), with labels to the features discussed in the text.

The most prominent feature of the giant branch is the Red Clump (RC in Fig. 10, around $G_{BP} - G_{RP}$= 1.2, M_G = 0.5 mag). It corresponds to low-mass stars that burn helium in their core (e.g. Girardi 2016). The colour of core-helium burning stars is strongly dependent on metallicity and age. The more metal-rich, the redder, which leads to this red clump feature in the local HRD. For more metal-poor populations, these stars are bluer and lead to the horizontal-branch (HB) feature that is clearly visible in globular clusters (Fig. 11).

The secondary red clump (SRC in Fig. 10, around $G_{BP} - G_{RP} = 1.1$, $M_G = 0.6$) is more extended in its bluest part to fainter magnitudes than the red clump. It corresponds to younger more massive red clump stars (Girardi 1999) and is therefore mostly visible in the local HRD (Fig. 6c). Core-helium burning stars that are even more massive are more luminous than the red clump and lie still on the blue part of it, leading to a vertical structure that is sometimes called the Vertical Red Clump (VRC in Fig. 10).

On the red side and fainter than the clump lies the RGB bump (RGBB in Fig. 10). This bump is caused by a brief interruption of the stellar luminosity increase as a star evolves on the red giant branch by burning its hydrogen shell, which creates an accumulation of stars at this HRD position (e.g. Christensen-Dalsgaard 2015). Its luminosity changes more with metallicity and age than the red clump. Brighter than the red clump, at $M_G \sim -0.5$, lies the AGB bump (AGBB in Fig. 10), which corresponds to the start of the asymptotic giant branch (AGB) where stars are burning their helium shell (e.g. Gallart 1998). The AGB bump is much less densely populated than the RGB bump. It is also clearly visible in the HRD of 47 Tuc (Fig. 11a).

The globular clusters in Fig. 11 clearly illustrate the diversity of the HB morphology. Some have predominantly blue HB (NGC 6397), some just red HB (NGC 104), and some a mixed HB showing bimodal distribution (NGC 5272 and NGC 6362). The HB morphology is explained in the framework of the multiple populations; it is regulated by age, metallicity, and first/second generation abundances (Carretta et al. 2009). NGC 6362 is the least massive globular that presents multiple populations. Mucciarelli et al. (2016) concluded that most of the stars that populate the red HB are Na poor and belong to the first generation, while the blue side of the HB is populated by the Na-rich stars belonging to the second generation. The same kind of correlation is shown in general by the globular clusters. We quote among others the studies of 47 Tuc (Gratton et al. 2013) and NGC 6397 (Carretta et al. 2009). The role of the He abundances is still under discussion (Marino et al. 2014; Valcarce et al. 2016). He-enhanced stars are indeed expected to populate the blue side of the instability strip because they are still O depleted and Na enhanced, as observed in the second-generation stars. How significant the He enhancement is still unclear.

Figure 3 shows that the globular cluster HB can extend towards the extreme horizontal branch (EHB) region. They are in the same region of the HRD as the hot subdwarfs, which creates a clump at $M_G = 4$ and $G_{BP} - G_{RP} = -0.5$ that is well visible in Figs. 1 and 5. These stars are also nicely characterised in terms of variability, including binary-induced variability, in Gaia Collaboration (2018b). These hot subdwarfs are considered to be red giants that lost their outer hydrogen layers before the core began to fuse helium, which might be due to the interaction with a low-mass companion, although other processes might be at play (e.g. Heber 2009). *Gaia* will allow detailed studies of the differences between cluster and field hot subdwarfs.

4.4. Planetary nebulae

At the end of the AGB phase, the star has lost most of its hydrogen envelope. The gas expands while the central star first grows hotter at constant luminosity, contracting and fusing hydrogen in the shell around its core (post-AGB phase), then it slowly cools when the hydrogen shell is exhausted, to reach the white dwarf phase. This planetary nebulae phase is very short, about 10 000 yr, and is therefore quite difficult to observe in the HRD. The *Gaia* DR2 contains many observations of nearby planetary nebulae as their expanding gas create excess flux over the mean sky background that triggers the on-board detection. We here wish to follow the route of the central star in the HRD. While some central planetary nebula stars are visible in the Galactic Pole HRD (Fig. 12), post-AGB stars are too rare to appear in this diagram. We used catalogue compilations to highlight the position of the two types in the *Gaia* HRD.

We used the Kerber et al. (2003) catalogue of Galactic planetary nebulae, selecting only sources classified as central stars that are clearly separated from the nebula. With a cross-match radius of 1″ and using all our filter criteria of Sect. 2.1, only four stars remain. We therefore relaxed the extinction criteria to $E(B-V) < 0.05$ and the parallax relative uncertainty to $\sigma_\varpi/\varpi <$ 20%, leading to 23 stars.

For post-AGB stars, we used the catalogue of Szczerba et al. (2007) and the 2MASS identifier provided for the cross-match. We selected only stars that are classified as very likely post-AGB objects. Here we also relaxed the extinction criteria to $E(B-V) < 0.05$ and the parallax relative uncertainty to $\sigma_\varpi/\varpi <$ 20%, leading to 11 stars.

While some outliers are seen in Fig. 12, either due to cross-match or misclassification issues, the global position of these stars in the HRD closely follows the expected track from the AGB to the white dwarf sequence. We note that this path crosses the hot subdwarf region we discussed in the previous section.

5. White dwarfs

The Sloan Digital Sky Survey (SDSS, Ahn et al. 2012) has produced the largest spectroscopic catalogue of white dwarfs so far (e.g. Kleinman et al. 2013). This data set has greatly aided our understanding of white dwarf classification and evolution. For example, it has allowed determining the white dwarf mass distribution for large statistical samples of different white dwarf

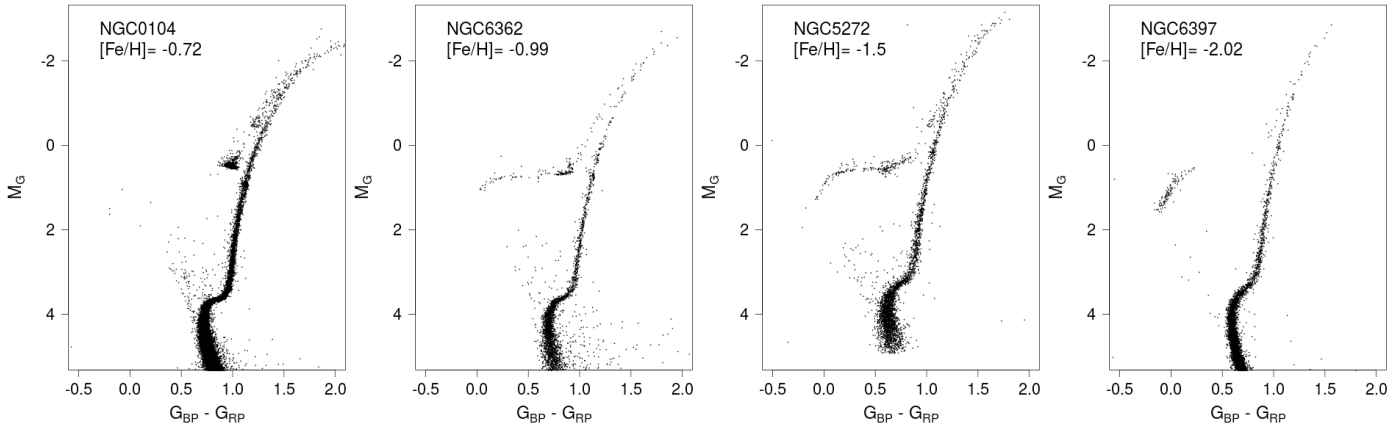

Fig. 11. Several globular clusters selected to show a clearly defined and very different horizontal branch, sorted by decreasing metallicity. *Panel a*: NGC 104 (47 Tuc), *panel b*: NGC 6362, *panel c*: NGC 5272, and *panel d*: NGC 6397.

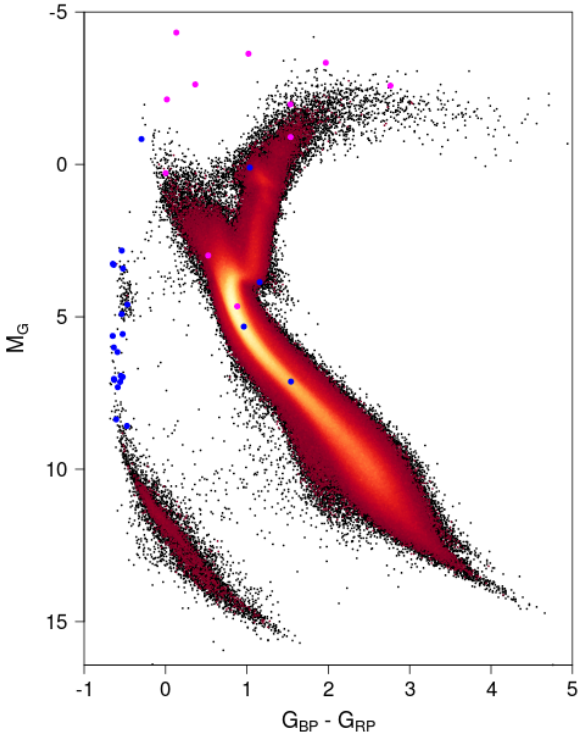

Fig. 12. North Galactic Pole HRD ($b > 50°$, 2 077 925 stars) with literature central planetary nebula stars (blue) and post-AGB stars (magenta).

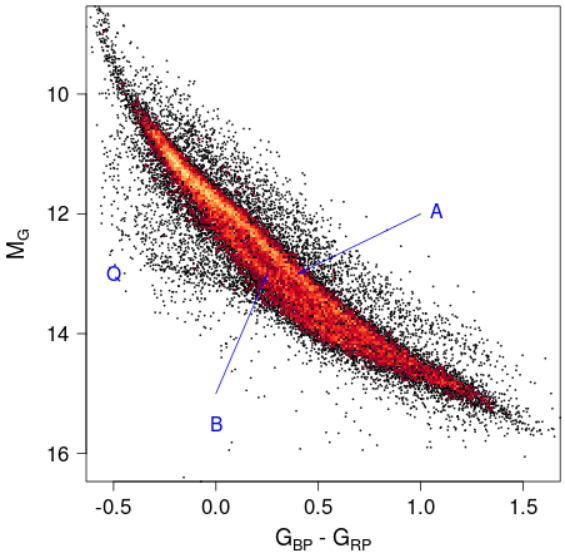

Fig. 13. *Gaia* HRD of white dwarfs with $\sigma_\varpi/\varpi < 5\%$ (26 264 stars), with letter labels to the features discussed in the text.

spectral types. However, much of this work is model dependent and relies upon theoretical mass-radius relationships and stellar atmosphere models, whose precision has only been tested in a limited way. These tests have been limited by the relatively small number of white dwarfs for which accurate parallaxes are available (e.g. Provencal et al. 1998) and by the precision of the parallaxes for these faint stars. This work was updated using the *Gaia* DR1 catalogue (Tremblay et al. 2017), which included more stars, but the uncertainties remain too large to constrain the theoretical mass-radius relations. Only in a few cases, where the white dwarf resides in a binary system, have mass radius measurements begun to approach the accuracy required to constrain the core composition and H layer mass of individual stars (e.g. Barstow et al. 2005; Parsons et al. 2017; Joyce et al. 2017). Even then, some of these white dwarfs may not be representative of the general population because common envelope evolution may have caused them to depart from the normal white dwarf evolutionary paths.

The publication of *Gaia* DR2 presents the opportunity to apply accurate parallaxes, with uncertainties of 1% or smaller, to the study of white dwarf stars. The availability of these data, coupled with the accurate *Gaia* photometry, yields the absolute magnitude, with which the white dwarfs can be clearly located in the expected region of the HRD (Figs. 5 and 6). Figure 13 shows the white dwarf region of the HRD alone. This sample was selected with $G_{\rm BP} - G_{\rm RP} < 2$ and $G - 10 + 5\log_{10}\varpi > 10 + 2.6\,(G_{\rm BP} - G_{\rm RP})$ and by applying the filters described in Sect. 2, including the low-extinction $E(B-V) < 0.015$ criterion, but with a stronger constraint on the parallax relative uncertainty of 5%. This yields a catalogue of 26 264 objects. We overplot in Fig. 14 white dwarf evolutionary models[3] for C/O cores (Holberg & Bergeron 2006; Kowalski & Saumon 2006; Tremblay et al. 2011; Bergeron et al. 2011) with colours computed using the revised *Gaia* DR2 passbands (Evans et al. 2018).

Several features are clearly visible in Fig. 13. First there is a clear main concentration of stars that is distributed continuously

[3] http://www.astro.umontreal.ca/~bergeron/CoolingModels

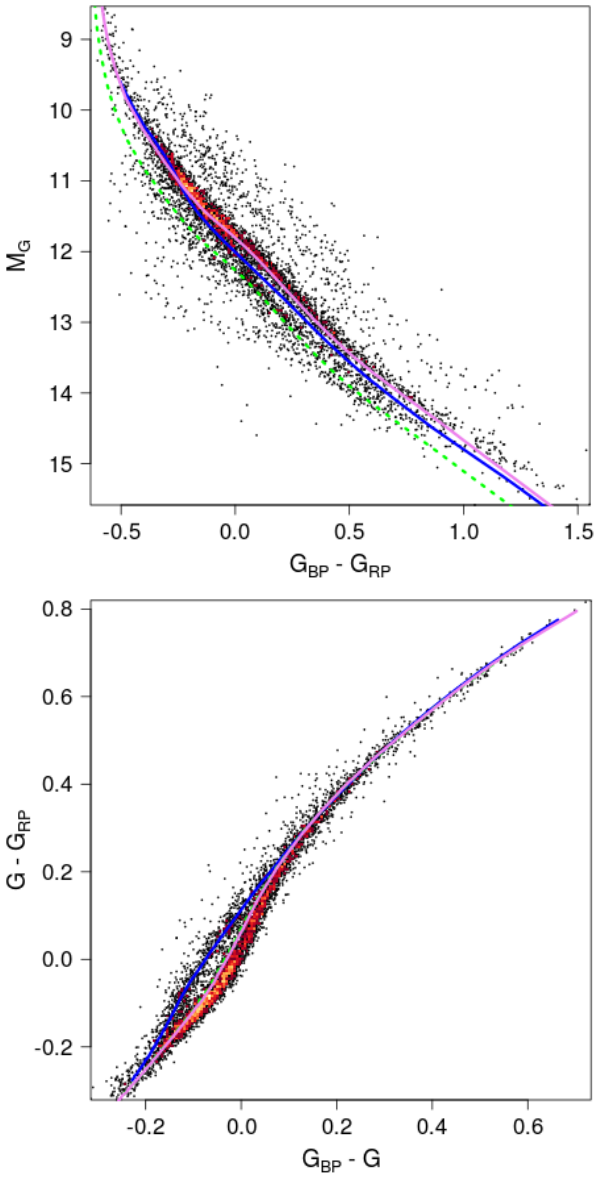

Fig. 14. *Gaia* HRD of white dwarfs with $\sigma_\varpi/\varpi < 5\%$ and $\sigma_{G_{BP}} < 0.01$ and $\sigma_{G_{RP}} < 0.01$ (5 781 stars) overlaid with white dwarf evolutionary models. Magenta: 0.6 $M_\odot$ pure H; green dashed: 0.8 $M_\odot$ pure H; and blue: 0.6 $M_\odot$ pure He. *Panel a*: HRD. *Panel b*: colour–colour diagram.

from left to right in the diagram (A) and coincides with the 0.6 $M_\odot$ hydrogen evolutionary tracks (in magenta). This is expected because the white dwarf mass distribution peaks very strongly near 0.6 $M_\odot$ (Kleinman et al. 2013). Interestingly, the concentration of white dwarfs departs from the cooling tracks towards the red end of the sequence.

Just below the main 0.6 $M_\odot$ concentration of white dwarfs is a second, separate concentration (B) that seems to be separate from the 0.6 $M_\odot$ peak at $G_{BP} - G_{RP} \sim -0.1$ before again merging by $G_{BP} - G_{RP} \sim 0.8$. At the maximum separation, this concentration is roughly aligned with the 0.8 $M_\odot$ hydrogen white dwarf cooling track (in green), which is not expected. While the SDSS mass distribution (Kleinman et al. 2013) shows a significant upper tail that extends through 0.8 $M_\odot$ and up to almost 1.2 $M_\odot$, there is no evidence for a minimum between 0.6 and 0.8 $M_\odot$ like that seen in Fig. 14a. A mass difference should therefore not lead to this feature. However, for a given mass, the evolutionary tracks for different compositions (DA: hydrogen and DB: helium) and envelope masses are virtually coincident at the resolution of Fig. 14 in the theoretical tracks, leading to no direct interpretation from the tracks in the HRD alone, but we describe below a different view from the colour–colour relation and the SDSS comparison.

A third, weaker concentration of white dwarfs in Fig. 13 lies below the main groups (Q). It does not follow an obvious evolutionary constant mass curve, which would be parallel to those shown in the plot. Beginning at approximately $M_G = 13$ and $G_{BP} - G_{RP} = -0.3$, it follows a shallower curve that converges with the other concentrations near $G_{BP} - G_{RP} = 0.2$.

White dwarfs are also seen to lie above the main concentration A. This can be explained as a mix between natural white dwarf mass distributions and binarity (see Fig. 8).

Selecting only the most precise G_{BP} and G_{RP} photometry ($\sigma_{G_{BP}} < 0.01$ and $\sigma_{G_{RP}} < 0.01$), we examined the colour–colour relation in Fig. 14b. The sequence is also split into two parts in this diagram. We verified that the two splits coincide, meaning that the stars in the lower part of Fig. 14a lie in the upper part of Fig. 14b. The mass is not expected to lead to significant differences in this colour–colour diagram, and the theoretical tracks coincide with the observed splits, pointing towards a difference between helium and hydrogen white dwarfs. It also recalls the split in the SDSS colour–colour diagram (Harris et al. 2003).

While *Gaia* identifies white dwarfs based on their location on the HRD, SDSS white dwarfs were identified spectroscopically, providing further information on the spectral type, $T_{\rm eff}$, and $\log g$ as well as a classification. Therefore we cross-matched the two data sets to better understand the features observed in Fig. 14.

We obtained a catalogue of spectroscopically identified SDSS white dwarfs from the Montreal White Dwarf Database[4] (Dufour et al. 2017) by downloading the whole catalogue and then filtering for SDSS identifier, which yielded 28 797 objects. Using the SDSS cross-match provided in the *Gaia* archive (Marrese et al. 2018), we found that there are 22 802 objects in common and 5 237 satisfying all the filters described in Sect. 2.1 and with single-star spectral type information. Figure 15 shows the SDSS $u - g$ colour magnitude for the sample with the absolute u magnitude calculated using the *Gaia* parallax. The distribution is clearly bifurcated. Evolutionary tracks for H and He atmospheres (0.6 $M_\odot$) are overplotted in the figure, indicating that this is due to the different atmospheric compositions. The *Gaia* counterparts of these SDSS white dwarfs are quite faint, and therefore the features seen in Fig. 14a are less well visible in this sample because of the larger noise in the parallaxes and the colours. Still, it allowed us to verify that the split of the SDSS white dwarfs corresponds to the location of the *Gaia* splits in Fig. 14. The narrower filter bands of SDSS are more sensitive to atmospheric compositions than the broad BP and RP *Gaia* bands. In particular, the u -band fluxes of H-rich DA white dwarfs are suppressed by the Balmer jump at 364.6 nm, which reddens the colours of these stars. The Balmer jump is in the wavelength range where the *Gaia* filters calibrated for DR2 differ most from the nominal filters (Evans et al. 2018), which explains the importance of using tracks that are updated to the DR2 filters for the white dwarf studies instead of the nominal tracks provided by Carrasco et al. (2014).

Figure 16 shows the colour-magnitude diagrams in the *Gaia* and SDSS photometry bands, overlaid with the white dwarfs for specific spectral types. The locations of the various spectral types correspond well to the expected colours arising from their effective temperatures. For example, DQ (carbon), DZ (metal

[4] http://www.montrealwhitedwarfdatabase.org/

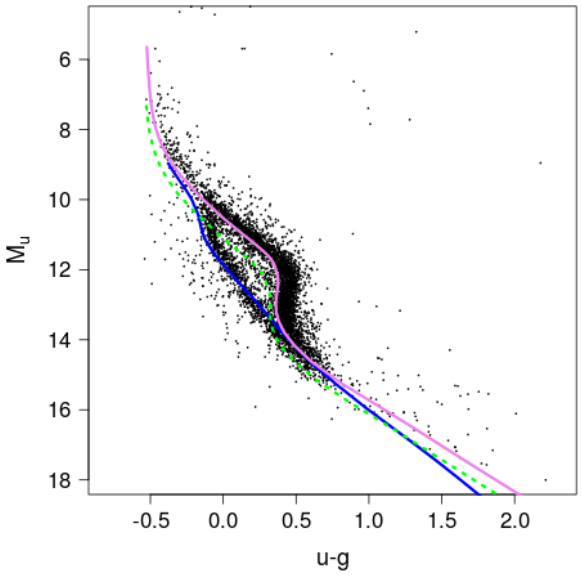

Fig. 15. SDSS white dwarfs (5237 stars) with evolutionary models. M_u is computed using the SDSS u magnitude and the *Gaia* parallax. Magenta: 0.6 $M_\odot$ pure H; green dashed: 0.8 $M_\odot$ pure H; and blue: 0.6 $M_\odot$ pure He.

rich), and DC (no strong lines) stars are confined to the red end of the colour-magnitude diagram, while the DO stars (ionised helium) all lie at the blue end. DAs cover the whole diagram. Interestingly, in Fig. 16b, a significant number of classified DA white dwarfs appears to occupy the He-rich atmosphere branch that is indicated by the evolutionary track in Fig. 15. The weaker Q concentration seems to include stars of all types except for DO and DZ. However, the most numerous components are the DA and DQs.

6. Cluster as stellar parameter templates

Clusters have long been considered as benchmarks with regard to the determination of the stellar properties. Open cluster stars share common properties, such as age and chemical abundances. The level of homogeneity of open clusters has been assessed in several papers (Cantat-Gaudin et al. 2014; Bovy 2016). By means of a high-precision differential abundance analysis, the Hyades have been proved to be chemically in-homogeneous at the 0.02 dex level (Liu et al. 2016) at maximum. Until now, the study of clusters was hampered by the disk field contamination. This in turn results in difficult membership determination, and in highly uncertain parameters (Netopil et al. 2015). Distance and age, together with chemical abundances, are the fundamental properties for a meaningful description of the disk characteristics. Their study complements the field population studies that are based on Galactic surveys. Globular clusters are fundamental tools for studying the properties of low-mass stars and the early chemical evolution of the Galaxy. Now *Gaia* DR2 data bring us into a completely new domain. High-accuracy parallaxes and exquisite photometry make the comparison with theoretical isochrones very fruitful, based on which, stellar properties can be defined. A detailed discussion of the uncertainties of stellar models is beyond the scope of this paper. Here we would like to recall that effects such as convection in the stellar core, mass loss, rotation, and magnetic fields are still poorly constrained and are often only parametrised in stellar models (Weiss & Heners 2013; Bell 2016; Pasetto et al. 2016). Although very significant, seismic predictions depend on our poor knowledge

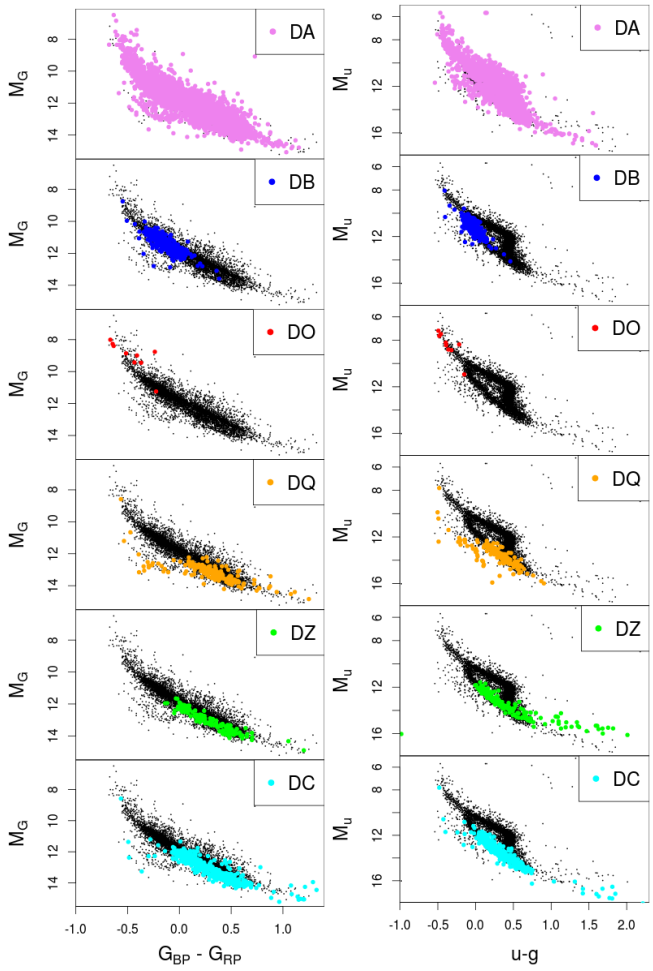

Fig. 16. SDSS white dwarfs per spectral type (DA: hydrogen; DB: neutral helium; DO: ionised helium; DQ: carbon; DZ: metal rich; and DC: no strong lines). *Left*: *Gaia* photometry (*panel a*), and *right*: SDSS photometry (*panel b*).

of the relevant physics (Miglio et al. 2015). A calibration of these effects on star cluster photometry is mandatory and will complement asteroseismology as a tool for testing stellar physics and will ultimately improve stellar models. In Table 2 we present the ages and the extinction values derived by isochrone fitting for the sample of open clusters discussed in this paper. The uncertainties are $\Delta(\log(\text{age}))$ $^{+0.14}_{-0.22}$, $^{+0.11}_{-0.13}$, $^{+0.08}_{-0.06}$ for $6 < \log(\text{age}) \leq 7$, $7 < \log(\text{age}) \leq 8$, $\log(\text{age}) > 8$, respectively, and $\Delta E(B-R) = 0.04$. Here we made use of PARSEC isochrones (Chen et al. 2014) for metallicities $Z = 0.017$ and $Z = 0.020$ updated to the latest transmission curve calibrated on *Gaia* DR2 data (Evans et al. 2018)[5]. Praesepe, Hyades, Alpha Per, and NGC 6475 were fitted with $Z = 0.02$ (Kharchenko et al. 2015; Gaia Collaboration 2017), while the others were reproduced using $Z = 0.017$. This gave a relatively poor fit for clusters that are known to have subsolar metallicity, such as NGC 2158, which has [Fe/H] = −0.25 (Kharchenko et al. 2015). The PARSEC solar value is $Z = 0.015$. This version of the PARSEC tracks makes use of a modified relation between the effective temperature and Rosseland mean optical depth τ across the atmosphere that is derived from PHOENIX (Allard et al. 2012) and in particular from the set of BT-Settl models. With this modified relation, introduced to better reproduce the observed mass-radius relation in nearby low

[5] PARSEC isochrones in *Gaia* DR2 passbands are available at http://stev.oapd.inaf.it/cgi-bin/cmd

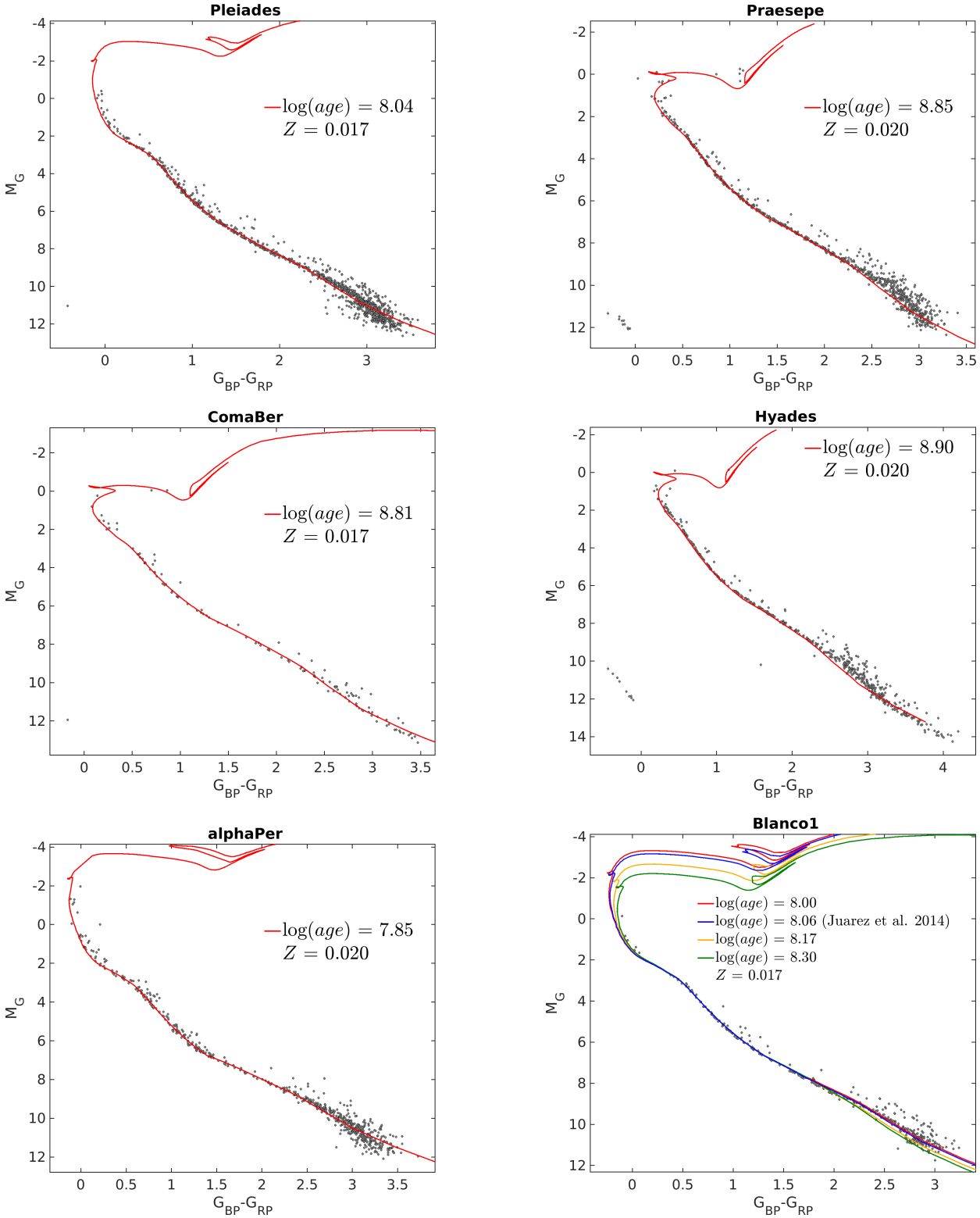

Fig. 17. HRDs of nearby clusters compared with PARSEC isochrones (see text for details) of the Pleiades (*panel a*), Praesepe (*panel b*), Coma Ber (*panel c*), Hyades (*panel d*), Alpha Per (*panel e*), and Blanco 1 (*panel f*). Praesepe, Hyades, and Alpha Per are fitted with $Z = 0.02$, while the others are reproduced using $Z = 0.017$.

mass stars (Chen et al. 2014), the models provide a good representation of the colour distribution of very low mass stars in several passbands.

Figure 17 shows the HRD of a few nearby open clusters compared with PARSEC isochrones. The distance modulus (Table 2) was used, and the extinction was not corrected in the photometry, but was applied on the isochrones.

The fits are remarkably good in the upper and lower main sequence. The high quality of *Gaia* photometry produces well-defined features, very clean main sequences, and a clear

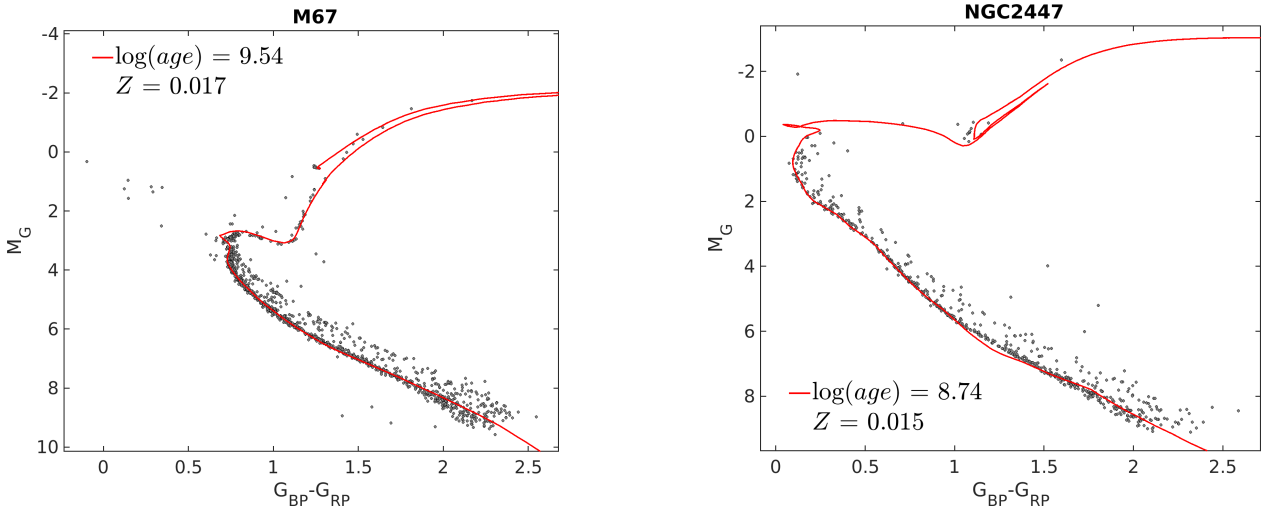

Fig. 18. HRDs of two distant clusters compared with PARSEC isochrones (see text for details): M67 (NGC 2682) (*panel a*), and NGC 2447 (*panel b*).

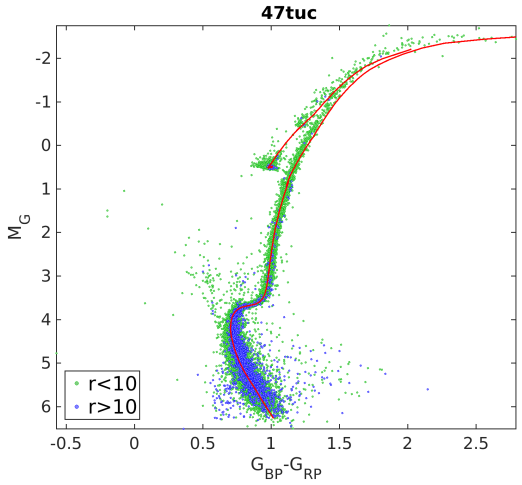

Fig. 19. HRD of the globular cluster 47 Tuc compared with PARSEC isochrones (see text for details). The inner region (radius < 10 arcmin, e.g. three times the half-light radius) is shown in green, while the external regions are plotted in blue. A maximum radius of 1.1 degrees was used.

definition of the binary sequence. The agreement for the Pleiades is particularly remarkable. In spite of the impressively good agreement across a range of several magnitudes, at about $M_G \sim 10$, the model predictions and the observed main sequence still disagree. The slope of the theoretical main sequence initially seems to be slightly steeper than the observed main sequence, while at even lower magnitudes, the slope of the observed main sequence becomes steeper than the predicted main sequence. The latter effect might be due to the background subtraction, which becomes challenging at these faint magnitudes (Evans et al. 2018; Arenou et al. 2018). Instead, the initial steepening of the isochrones, which is also observed in other clusters in Fig. 17, might indicate that the adopted boundary conditions in the domain of very low mass stars in PARSEC need a further small revision. It is well known that current models and the colour transformations fail to reproduce the main sequence in the very low mass regime (Bell 2016), and the data gathered by *Gaia* will certainly help to overcome this long-standing problem.

The age determination of Blanco 1 deserves further comments. Blanco 1 has a slightly super-solar metallicity [Fe/H] = +0.04 ± 0.04 (Ford et al. 2005). Previous age determination placed Blanco 1 in the age range log(age) = 8.0–8.17 (Moraux et al. 2007). A determination of the lithium depletion boundary on very low mass stars gives log(age) = 8.06 ± 0.13 when a correction for magnetic activity is applied (Juarez et al. 2014). From the main-sequence turnoff, we obtain log(age) = 8.30. However, fitting the main-sequence turnoff in such an inconspicuous cluster might not lead to correct results, since the initial mass function disfavours higher mass stars. Using the lithium depletion boundary age of log(age) of 8.06 ± 0.04, we reproduce the lower main sequence, with a marginal fit to the upper main sequence. Similar considerations apply to the Pleiades, whose log(age) is in the range 8.04 ± 0.03–8.10 ± 0.06 and is derived from the lithium depletion boundary or from eclipsing binaries (for a recent discussion, see David et al. 2016). Using the lithium depletion boundary age of 8.04 ± 0.06, we can reproduce the main sequence with PARSEC isochrones.

Figure 18 presents the comparison of two distant clusters, NGC 2682 (M67) and NGC 2447, with PARSEC isochrones. M 67 is one of the best-studied star clusters. It has a metallicity near solar, an accessible distance of about 1028 pc with low reddening (Taylor 2007), and an age close to solar (~4 Gyr). It is a very highly populated object that includes over 1000 members from main-sequence dwarfs, a well-populated subgiant and red giant branch, white dwarfs, blue stragglers, sub-subgiants, X-ray sources, and cataclysmic variables. *Gaia* identifies 1526 members. It was observed by almost all the most relevant spectroscopic surveys (*Gaia* -ESO, APOGEE, WIYN, etc.). Asteroseismologic data are available from the Kepler 2 mission (Stello et al. 2016). M67 is a cornerstone of stellar astrophysics, and it is a calibrator of age determination via gyrochronology (Barnes et al. 2016). Its turn-off mass is very close to the critical mass for the onset of core convection. For this reason, the cluster is especially interesting for this specific regime of stellar models and their dependence on different parameters such as nuclear reaction rate and solar abundances. The main-sequence termination presents a distinctive hook and a gap just above it. These features are used to distinguish between diffusive and non-diffusive evolutionary models. Atomic diffusion is very important for the morphology of isochrones in the vicinity of the turn-off. The hook feature traces the rapid contraction phase that occurs at central H exhaustion in those stars that have convective cores during their main-sequence phase. This hook is located at somewhat

higher luminosities and cooler temperatures when diffusive processes are included (Michaud et al. 2004). *Gaia* photometry and parallax place the location of these features very precisely in the HRD. PARSEC isochrones, including overshoot and diffusion, reproduce the main-sequence slope and termination point reasonably well, although additional overshoot calibration might be necessary. A population of blue stragglers, a few yellow giants, and two sub-subgiants are clearly visible among the members. The binary star sequence in M67 is clearly defined as well.

NGC 2447 is a younger object with an age of 0.55 Gyr and almost solar metallicity. Previous photometry is relatively poor (Clariá et al. 2005). In *Gaia* DR2, photometry and membership of the cluster stand out very clearly. PARSEC isochrones reproduce the main sequence very well, while the red clump colour is slightly redder.

Figure 19 presents the HRD of the globular cluster 47 Tuc (see Table 3), which is one prominent example of multiple populations in globular clusters. *Hubble* Space Telescope (HST) photometry in the blue passbands has revealed a double main sequence (Milone et al. 2012) and distinct subgiant branches (Anderson et al. 2009). These components are not visible in the high-accuracy *Gaia* photometry, since bluer colours would be necessary. 47 Tuc has a relatively high average metallicity of [Fe/H] = −0.72. We fit it with PARSEC isochrones with $Z = 0.0056$, $Y = 0.25$. Since no alpha-enhanced tracks are available in the PARSEC data set, we use the Salaris et al. (1993) relation to account for the enhancement.

7. Variation of the HRD with kinematics

Thin disk, thick disk, and halo have different age and metallicity distributions as well as kinematics. The *Gaia* HRD is therefore expected to vary with the kinematics properties. For stars with radial velocities, we apply classical cuts to broadly kinematically select thin-disk ($V_{\rm tot} < 50\,{\rm km\,s^{-1}}$), thick-disk ($70 < V_{\rm tot} < 180\,{\rm km\,s^{-1}}$), and halo stars ($V_{\rm tot} > 200\,{\rm km\,s^{-1}}$) (e.g. Bensby et al. 2014), using U,V,W computed within the framework of Gaia Collaboration (2018d), in which a global Toomre diagram is presented. This sample with radial velocities is limited to bright stars. To probe deeper into the HRD, we also made a selection using only tangential velocities, which we computed with $V_T = 4.74/\varpi \sqrt{\mu_{\alpha*}^2 + \mu_\delta^2}$. We roughly adapted our kinematic cut to the fact that we now only have two components of the velocity instead of three: we used $V_T < 40\,{\rm km\,s^{-1}}$ for the thin disk and $60 < V_T < 150\,{\rm km\,s^{-1}}$ for the thick disk, but still $V_T > 200\,{\rm km\,s^{-1}}$ for the halo. To all our samples we also applied the $E(B-V) < 0.015$ selection criterion. The results are presented in Figs. 20 and 21. We note that hot star radial velocities are not included in *Gaia* DR2 (Sartoretti et al. 2018), which explains why they are missing in Fig. 20.

The left figures associated with the thin disk show the same main features typical of a young population as the local HRD of Fig. 6: young hot main-sequence stars are present (Fig. 21a), the secondary red clump as well as the AGB bump is visible (Fig. 20a), and the turn-off region is diffusely populated. The middle figures associated with the thick disk show a more localised turn-off typical of an intermediate to old population. The median locus of the main sequence is similar to the thin-disk selection. The right figures associated with the halo show an extended horizontal branch, typical of old metal-poor populations, but also two very distinct main sequences and turn-offs. We note the presence of the halo white dwarfs.

We study the kinematic selection associated with the halo in Fig. 22 in more detail. The two main-sequence turn-offs are shifted by ∼0.1 mag in colour. The red main-sequence turn-off is shifted by ∼0.05 mag from the thick-disk kinematic selection main sequence (green line in Fig. 22a). Comparison with isochrones clearly identifies the distinct main sequences as being driven by a metallicity difference of about 1 dex. To further confirm this, we cross-matched our selection with the APOGEE DR14 catalogue (Holtzman et al. 2015) using their 2MASS ID and the 2MASS cross-match provided in the *Gaia* archive (Marrese et al. 2018). There are 184 stars in common, 1168 if we relax the low-extinction criteria that mostly confine our HRD selection to the galactic poles. The metallicity distribution is indeed double-peaked, with peak metallicities of −1.3 and −0.5 dex. We superimpose in Fig. 22 the corresponding PARSEC isochrones using the Salaris et al. (1993) formula for the mean α enhancement of 0.23 for [M/H] = −1.3 and −0.5 and ages of 13 and 11 Gyr, respectively. While the extent of the horizontal branch does not correspond to the isochrones used here, it can be compared to the empirical horizontal branches of the globular clusters presented in Fig. 11.

This bimodal metallicity distribution in the kinematic selection of the halo may recall the globular cluster bimodal metallicity distribution with the same peaks at [Fe/H] ∼ −0.5 and [Fe/H] ∼ −1.5 (e.g. Zinn 1985), the more metal-rich part being associated with the thick disk and bulge. We verified with the globular cluster kinematics provided in Gaia Collaboration (2018c) that 80% of these globular clusters indeed fall into our halo kinematic selection, independently of their metallicity. The −0.5 dex peak also recalls the bulge metal-poor component (e.g. Hill et al. 2011). However, it seems to be different from the double halo found at larger distances (Carollo et al. 2007; de Jong et al. 2010): while their inner-halo component at ∼−1.6 could correspond to our metal-poor component, their metal-poor component is at metallicity ∼−2.2 and is found in the outer Galaxy. This duality in the metallicity distribution of the kinematically selected halo stars has also been found using TGAS data with RAVE and APOGEE (Bonaca et al. 2017). Half of the stars are also found to have [M/H] > −1 dex with a dynamically selected halo sample in TGAS/RAVE by Posti et al. (2018).

The α abundances of this APOGEE sample (Fig. 22b) let us recover the two sequences described by Nissen & Schuster (2010) using an equivalent kinematic selection. We adjusted a median spline to the main sequence of the high-velocity HRD and present the velocity distribution of the stars on either side of this median spline in Fig. 22c. The magenta sequence looks like a velocity distribution tail towards high velocities, while the blue sequence has a flat velocity distribution. We do not see any difference in the sky distribution of these components, most probably because the sky distribution is fully dominated by our sample selection criteria. All these tests and comparisons with the literature seem to indicate a very different formation scenario for the two components of this kinematic selection of the halo.

8. Summary

The unprecedented all-sky precise and homogeneous astrometric and photometric content of *Gaia* DR2 allows us to see fine structures in both field star and cluster HRD to an extent that has never been reached before. We have described the main filtering of the data that is required for this purpose and provided membership for a selection of open clusters covering a wide range of ages.

The variations with age and metallicity are clearly illustrated by the main sequence and the giant branches of a large set of

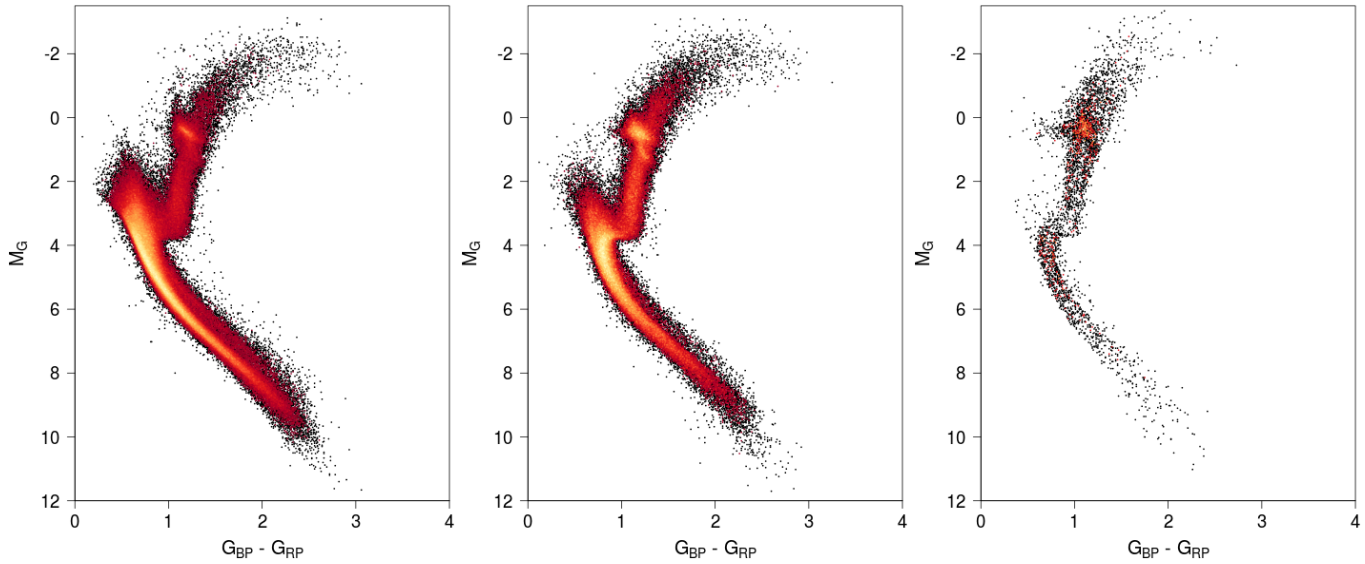

Fig. 20. *Gaia* HRDs with kinematic selections based on the total velocity: *panel a*: $V_{\rm tot} < 50\,{\rm km\,s^{-1}}$ (275 595 stars), *panel b*: $70 < V_{\rm tot} < 180\,{\rm km\,s^{-1}}$ (116 198 stars), and *panel c*: $V_{\rm tot} > 200\,{\rm km\,s^{-1}}$ (4461 stars).

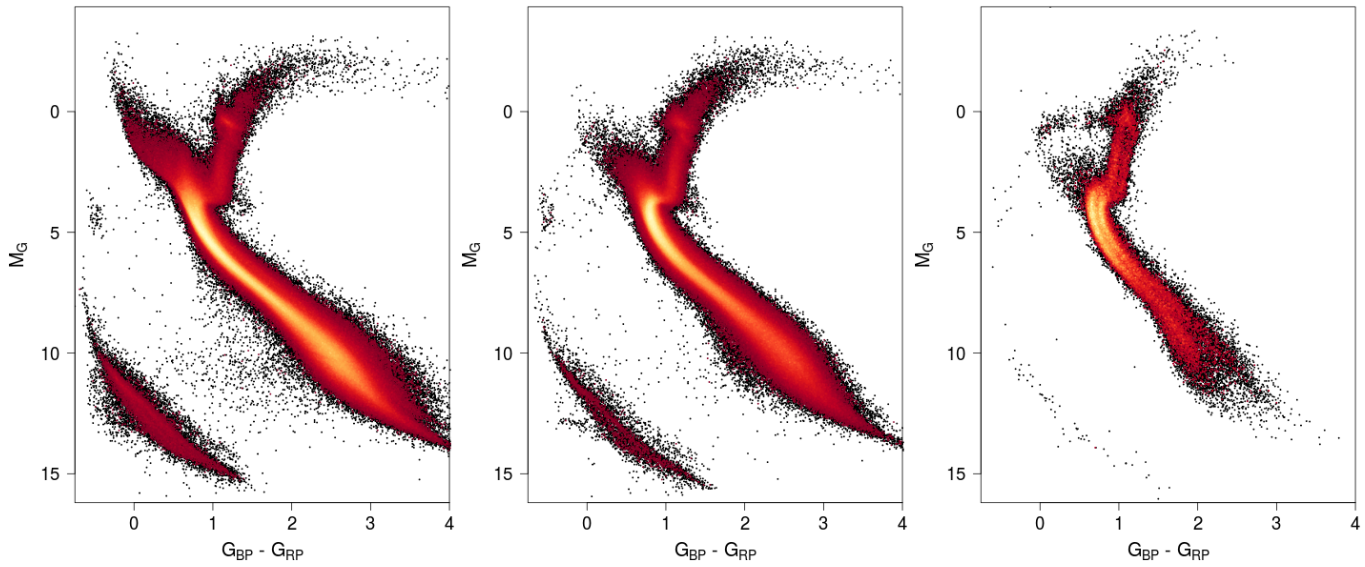

Fig. 21. *Gaia* HRDs with kinematic selections based on the tangential velocity: *panel a*: $V_T < 40\,{\rm km\,s^{-1}}$ (1 893 677 stars), *panel b*: $60 < V_T < 150\,{\rm km\,s^{-1}}$ (1 303 558 stars), and *panel c*: $V_T > 200\,{\rm km\,s^{-1}}$ (64 727 stars).

open and globular clusters and kinematically selected stellar populations. The main sequence for nearby stars is extremely thin, for field and cluster stars both, with a clear scattering of double stars up to 0.75 magnitude visible above the main sequence. *Gaia* DR2 provides a very unique view of the bottom of the main sequence down to the brown dwarf regime, including L-type and halo BDs. We also see the post-AGB stars and the central stars of planetary nebulae, which follow the expected tracks down to the white dwarf sequence, as well as hot subdwarfs.

The split in the white dwarf sequence between hydrogen and helium white dwarfs, which was first detected in the SDSS colour–colour diagrams, is visible for the first time in an HRD, with very thin sequences that agree with the strong peak of their mass distribution around 0.6 $M_\odot$.

Kinematic selections clearly show the change in HRDs with stellar populations. It highlights the strong bimodality of the HRD of the classical halo kinematic selection, and gives evidence of two very different populations within this selection.

All the features in the *Gaia* HRDs chiefly agree in general with the theoretical stellar evolution models. The differences that are observed for the faintest brown dwarfs, the white dwarf hydrogen/helium split, or the very fine structures of the open cluster main sequences, for example, are expected to bring new insight into stellar physics.

Numerous studies by the community are expected on the *Gaia* HRD. For example, rare stages of evolution will be extracted from the archive, together with more clusters, and detailed comparisons with different stellar evolution models will be made. The completeness of the data is a difficult question that we did not discuss here, but that will be studied by the community as it is a very important issue, in particular for determining the local volume density and all the studies of the initial mass function and stellar evolution lifetimes.

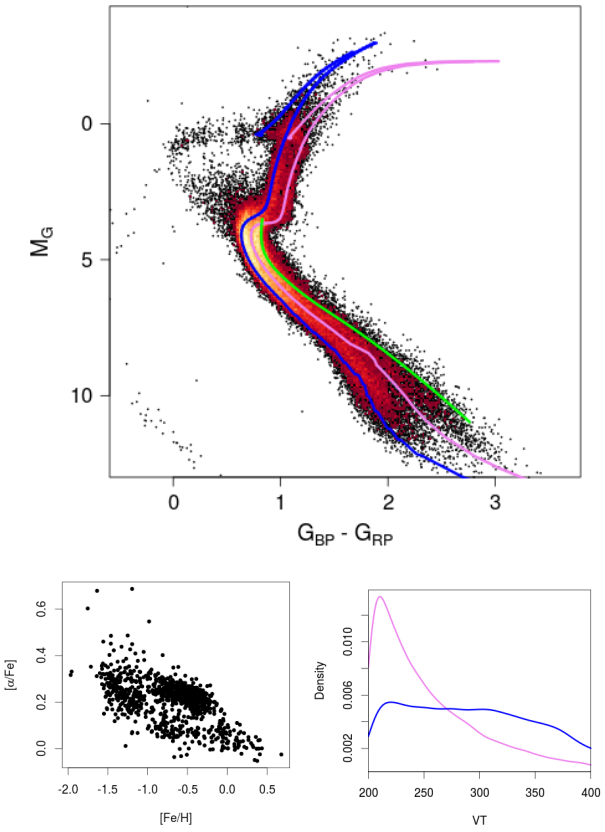

Fig. 22. *Panel a*: same as Fig. 21c (kinematic selection $V_T > 200\,\mathrm{km\,s^{-1}}$) overlaid with PARSEC isochrones for [M/H] = −1.3, age= 13 Gyr (blue), and [M/H] = −0.5, age = 11 Gyr (magenta) and [α/Fe] = 0.23; green line: median spline fit to the main sequence of the thick-disk kinematic selection (Fig. 21b). *Panel b*: [α/Fe] vs. [Fe/H] of the corresponding APOGEE stars without extinction criterion applied. *Panel c*: density distribution of the tangential velocity V_T on the blue and red sides of a median spline main-sequence fit.

The next *Gaia* release, DR3, will again be a new step for stellar studies. This will be achieved not only by the increase in completeness, precision, and accuracy of the data, but also by the additional spectrophotometry and spectroscopy, together with the binarity information that will be provided.

Acknowledgements. We thank Pierre Bergeron for providing the WD tracks in the *Gaia* DR2 passbands. This work presents results from the European Space Agency (ESA) space mission *Gaia*. *Gaia* data are being processed by the *Gaia* Data Processing and Analysis Consortium (DPAC). Funding for the DPAC is provided by national institutions, in particular the institutions participating in the *Gaia* MultiLateral Agreement (MLA). The *Gaia* mission website is https://www.cosmos.esa.int/gaia. The *Gaia* archive website is https://archives.esac.esa.int/gaia. The *Gaia* mission and data processing have financially been supported by, in alphabetical order by country: the Algerian Centre de Recherche en Astronomie, Astrophysique et Géophysique of Bouzareah Observatory; the Austrian Fonds zur Förderung der wissenschaftlichen Forschung (FWF) Hertha Firnberg Programme through grants T359, P20046, and P23737; the BELgian federal Science Policy Office (BELSPO) through various PROgramme de Développement d'Expériences scientifiques (PRODEX) grants and the Polish Academy of Sciences – Fonds Wetenschappelijk Onderzoek through grant VS.091.16N; the Brazil-France exchange programmes Fundação de Amparo à Pesquisa do Estado de São Paulo (FAPESP) and Coordenação de Aperfeicoamento de Pessoal de Nível Superior (CAPES) – Comité Français d'Evaluation de la Coopération Universitaire et Scientifique avec le Brésil (COFECUB); the Chilean Dirección de Gestión de la Investigación (DGI) at the University of Antofagasta and the Comité Mixto ESO-Chile; the National Science Foundation of China (NSFC) through grants 11573054 and 11703065; the Czech-Republic Ministry of Education, Youth, and Sports through grant LG 15010, the Czech Space Office through ESA PECS contract 98058, and Charles University Prague through grant PRIMUS/SCI/17; the Danish Ministry of Science; the Estonian Ministry of Education and Research through grant IUT40-1; the European Commission's Sixth Framework Programme through the European Leadership in Space Astrometry (https://www.cosmos.esa.int/web/gaia/elsa-rtn-programme ELSA) Marie Curie Research Training Network (MRTN-CT-2006-033481), through Marie Curie project PIOF-GA-2009-255267 (Space AsteroSeismology & RR Lyrae stars, SAS-RRL), and through a Marie Curie Transfer-of-Knowledge (ToK) fellowship (MTKD-CT-2004-014188); the European Commission's Seventh Framework Programme through grant FP7-606740 (FP7-SPACE-2013-1) for the *Gaia* European Network for Improved data User Services (https://gaia.ub.edu/Twiki/bin/view/GENIUS/WebHome, GENIUS) and through grant 264895 for the *Gaia* Research for European Astronomy Training (https://www.cosmos.esa.int/web/gaia/great-programme, GREAT-ITN) network; the European Research Council (ERC) through grants 320360 and 647208 and through the European Union's Horizon 2020 research and innovation programme through grants 670519 (Mixing and Angular Momentum tranSport of massIvE stars – MAMSIE) and 687378 (Small Bodies: Near and Far); the European Science Foundation (ESF), in the framework of the *Gaia* Research for European Astronomy Training Research Network Programme (https://www.cosmos.esa.int/web/gaia/great-programme, GREAT-ESF); the European Space Agency (ESA) in the framework of the *Gaia* project, through the Plan for European Cooperating States (PECS) programme through grants for Slovenia, through contracts C98090 and 4000106398/12/NL/KML for Hungary, and through contract 4000115263/15/NL/IB for Germany; the European Union (EU) through a European Regional Development Fund (ERDF) for Galicia, Spain; the Academy of Finland and the Magnus Ehrnrooth Foundation; the French Centre National de la Recherche Scientifique (CNRS) through action "Défi MASTODONS", the Centre National d'Etudes Spatiales (CNES), the L'Agence Nationale de la Recherche (ANR) "Investissements d'avenir" Initiatives D'EXcellence (IDEX) programme Paris Sciences et Lettres (PSL∗) through grant ANR-10-IDEX-0001-02, the ANR "Défi de tous les savoirs" (DS10) programme through grant ANR-15-CE31-0007 for project "Modelling the Milky Way in the *Gaia* era" (MOD4Gaia), the Région Aquitaine, the Université de Bordeaux, and the Utinam Institute of the Université de Franche-Comté, supported by the Région de Franche-Comté and the Institut des Sciences de l'Univers (INSU); the German Aerospace Agency (Deutsches Zentrum für Luft- und Raumfahrt e.V., DLR) through grants 50QG0501, 50QG0601, 50QG0602, 50QG0701, 50QG0901, 50QG1001, 50QG1101, 50QG1401, 50QG1402, 50QG1403, and 50QG1404 and the Centre for Information Services and High Performance Computing (ZIH) at the Technische Universität (TU) Dresden for generous allocations of computer time; the Hungarian Academy of Sciences through the Lendület Programme LP2014-17 and the János Bolyai Research Scholarship (L. Molnár and E. Plachy) and the Hungarian National Research, Development, and Innovation Office through grants NKFIH K-115709, PD-116175, and PD-121203; the Science Foundation Ireland (SFI) through a Royal Society – SFI University Research Fellowship (M. Fraser); the Israel Science Foundation (ISF) through grant 848/16; the Agenzia Spaziale Italiana (ASI) through contracts I/037/08/0, I/058/10/0, 2014-025-R.0, and 2014-025-R.1.2015 to the Italian Istituto Nazionale di Astrofisica (INAF), contract 2014-049-R.0/1/2 to INAF dedicated to the Space Science Data Centre (SSDC, formerly known as the ASI Sciece Data Centre, ASDC), and contracts I/008/10/0, 2013/030/I.0, 2013-030-I.0.1-2015, and 2016-17-I.0 to the Aerospace Logistics Technology Engineering Company (ALTEC S.p.A.), and INAF; the Netherlands Organisation for Scientific Research (NWO) through grant NWO-M-614.061.414 and through a VICI grant (A. Helmi) and the Netherlands Research School for Astronomy (NOVA); the Polish National Science Centre through HARMONIA grant 2015/18/M/ST9/00544 and ETIUDA grants 2016/20/S/ST9/00162 and 2016/20/T/ST9/00170; the Portugese Fundação para a Ciência e a Tecnologia (FCT) through grant SFRH/BPD/74697/2010; the Strategic Programmes UID/FIS/00099/2013 for CENTRA and UID/EEA/00066/2013 for UNINOVA; the Slovenian Research Agency through grant P1-0188; the Spanish Ministry of Economy (MINECO/FEDER, UE) through grants ESP2014-55996-C2-1-R, ESP2014-55996-C2-2-R, ESP2016-80079-C2-1-R, and ESP2016-80079-C2-2-R, the Spanish Ministerio de Economía, Industria y Competitividad through grant AyA2014-55216, the Spanish Ministerio de Educación, Cultura y Deporte (MECD) through grant FPU16/03827, the Institute of Cosmos Sciences University of Barcelona (ICCUB, Unidad de Excelencia "María de Maeztu") through grant MDM-2014-0369, the Xunta de Galicia and the Centros Singulares de Investigación de Galicia for the period 2016-2019 through the Centro de Investigación en Tecnologías de la Información y las Comunicaciones (CITIC), the Red Española de Supercomputación (RES) computer resources at MareNostrum, and the Barcelona Supercomputing Centre – Centro Nacional de Supercomputación (BSC-CNS) through activities AECT-2016-1-0006, AECT-2016-2-0013, AECT-2016-3-0011, and AECT-2017-1-0020; the Swedish National Space Board (SNSB/Rymdstyrelsen); the Swiss State Secretariat for Education, Research, and Innovation through the ESA PRODEX programme, the Mesures d'Accompagnement, the Swiss Activités Nationales Complémentaires, and the

Swiss National Science Foundation; the United Kingdom Rutherford Appleton Laboratory, the United Kingdom Science and Technology Facilities Council (STFC) through grant ST/L006553/1, the United Kingdom Space Agency (UKSA) through grant ST/N000641/1 and ST/N001117/1, as well as a Particle Physics and Astronomy Research Council Grant PP/C503703/1. This publication has made use of SIMBAD and VizieR, both operated at the Centre de Données astronomiques de Strasbourg (CDS, http://cds.u-strasbg.fr/). This publication has made use of data products from the Two Micron All Sky Survey, which is a joint project of the University of Massachusetts and the Infrared Processing and Analysis Center/California Institute of Technology, funded by the National Aeronautics and Space Administration and the National Science Foundation. This publication has made use of data products from SDSS-III. The Funding for SDSS-III has been provided by the Alfred P. Sloan Foundation, the Participating Institutions, the National Science Foundation, and the U.S. Department of Energy Office of Science. The SDSS-III web site is http://www.sdss3.org/. SDSS-III is managed by the Astrophysical Research Consortium for the Participating Institutions of the SDSS-III Collaboration.

References

Ahn, C. P., Alexandroff, R., Allende Prieto, C., et al. 2012, ApJS, 203, 21
Allard, F., Homeier, D., & Freytag, B. 2012, Phil. Trans. R. Soc. London, Ser. A, 370, 2765
Anderson, J., Piotto, G., King, I. R., Bedin, L. R., & Guhathakurta, P. 2009, ApJ, 697, L58
Andrae, R., Fouesneau, M., Creevey, O., et al. 2018, A&A, 616, A8 (*Gaia* 2 SI)
Arenou, F., Luri, X., Babusiaux, C., et al. 2018, A&A, 616, A17 (*Gaia* 2 SI)
Baraffe, I., Homeier, D., Allard, F., & Chabrier, G. 2015, A&A, 577, A42
Barnes, S. A., Weingrill, J., Fritzewski, D., Strassmeier, K. G., & Platais, I. 2016, ApJ, 823, 16
Barstow, M. A., Bond, H. E., Holberg, J. B., et al. 2005, MNRAS, 362, 1134
Bell, C. P. M. 2016, in 19th Cambridge Workshop on Cool Stars, Stellar Systems, and the Sun (CS19), 102
Bensby, T., Feltzing, S., & Oey, M. S. 2014, A&A, 562, A71
Bergeron, P., Wesemael, F., Dufour, P., et al. 2011, ApJ, 737, 28
Bonaca, A., Conroy, C., Wetzel, A., Hopkins, P. F., & Kereš D. 2017, ApJ, 845, 101
Bovy, J. 2016, ApJ, 817, 49
Cantat-Gaudin, T., Vallenari, A., Zaggia, S., et al. 2014, A&A, 569, A17
Capitanio, L., Lallement, R., Vergely, J. L., Elyajouri, M., & Monreal-Ibero, A. 2017, A&A, 606, A65
Carollo, D., Beers, T. C., Lee, Y. S., et al. 2007, Nature, 450, 1020
Carrasco, J. M., Catalán, S., Jordi, C., et al. 2014, A&A, 565, A11
Carretta, E., Bragaglia, A., Gratton, R. G., et al. 2009, A&A, 505, 117
Castelli, F., & Kurucz, R. L. 2003, in Modelling of Stellar Atmospheres, eds. N. Piskunov, W. W. Weiss, & D. F. Gray, IAU Symp., 210, A20
Chen, Y., Girardi, L., Bressan, A., et al. 2014, MNRAS, 444, 2525
Christensen-Dalsgaard, J. 2015, MNRAS, 453, 666
Clariá, J. J., Piatti, A. E., Lapasset, E., & Parisi, M. C. 2005, Baltic Astron., 14, 301
Conrad, C., Scholz, R.-D., Kharchenko, N. V., et al. 2014, A&A, 562, A54
Danielski, C., Babusiaux, C., Ruiz-Dern, L., Sartoretti, P., & Arenou, F. 2018, A&A, 614, A19
David, T. J., Conroy, K. E., Hillenbrand, L. A., et al. 2016, AJ, 151, 112
de Jong, J. T. A., Yanny, B., Rix, H.-W., et al. 2010, ApJ, 714, 663
Denissenkov, P. A., VandenBerg, D. A., Kopacki, G., & Ferguson, J. W. 2017, ApJ, 849, 159
Dotter, A., Sarajedini, A., Anderson, J., et al. 2010, ApJ, 708, 698
Dufour, P., Blouin, S., Coutu, S., et al. 2017, in 20th European White Dwarf Workshop, eds. P.-E. Tremblay, B. Gaensicke, & T. Marsh, ASP Conf. Ser., 509, 3
Evans, D., Riello, M., De Angeli, F., et al. 2018, A&A, 616, A4 (*Gaia* 2 SI)
Faherty, J. K., Burgasser, A. J., Cruz, K. L., et al. 2009, AJ, 137, 1
Fitzpatrick, E. L., & Massa, D. 2007, ApJ, 663, 320
Ford, A., Jeffries, R. D., & Smalley, B. 2005, MNRAS, 364, 272
Gaia Collaboration (Brown, A. G. A., et al.) 2016, A&A, 595, A2
Gaia Collaboration (van Leeuwen, F., et al.) 2017, A&A, 601, A19
Gaia Collaboration (Brown, A. G. A., et al.) 2018a, A&A, 616, A1 (*Gaia* 2 SI)
Gaia Collaboration (Eyer, L., et al.) 2018b, A&A, submitted (*Gaia* 2 SI)
Gaia Collaboration (Helmi, A., et al.) 2018c, A&A, 616, A12 (*Gaia* 2 SI)
Gaia Collaboration (Katz, D., et al.) 2018d, A&A, 616, A11 (*Gaia* 2 SI)
Gallart, C. 1998, ApJ, 495, L43
Girardi, L. 1999, MNRAS, 308, 818
Girardi, L. 2016, ARA&A, 54, 95
Gliese, W., & Jahreiß, H. 1991, in The Astronomical Data Center CD-ROM: Selected Astronomical Catalogs, eds. L. E. Brotzmann, & S. E. Gesser (Greenbelt: NASA Goddard Space Flight Center), 1
Gratton, R. G., Lucatello, S., Sollima, A., et al. 2013, A&A, 549, A41
Harris, H. C., Liebert, J., Kleinman, S. J., et al. 2003, AJ, 126, 1023
Harris, W. E. 1996, AJ, 112, 1487
Heber, U. 2009, ARA&A, 47, 211
Henry, T. J., & Jao, W.-C. 2015, IAU General Assembly, 22, 2253773
Hill, V., Lecureur, A., Gómez, A., et al. 2011, A&A, 534, A80
Holberg, J. B., & Bergeron, P. 2006, AJ, 132, 1221
Holtzman, J. A., Shetrone, M., Johnson, J. A., et al. 2015, AJ, 150, 148
Hurley, J., & Tout, C. A. 1998, MNRAS, 300, 977
Jordi, C., Gebran, M., Carrasco, J. M., et al. 2010, A&A, 523, A48
Joyce, S. R. G., Barstow, M. A., Casewell, S. L., Holberg, J. B., & Bond, H. E. 2017, in 20th European White Dwarf Workshop, eds. P.-E. Tremblay, B. Gaensicke, & T. Marsh, ASP Conf. Ser., 509, 389
Juarez, A. J., Cargile, P. A., James, D. J., & Stassun, K. G. 2014, ApJ, 795, 143
Kerber, F., Mignani, R. P., Guglielmetti, F., & Wicenec, A. 2003, A&A, 408, 1029
Kharchenko, N. V., Piskunov, A. E., Röser, S., Schilbach, E., & Scholz, R.-D. 2005, A&A, 438, 1163
Kharchenko, N. V., Piskunov, A. E., Schilbach, E., Roeser, S., & Scholz, R.-D. 2015, VizieR Online Data Catalog: J/A+A/585/A101
Kleinman, S. J., Kepler, S. O., Koester, D., et al. 2013, ApJS, 204, 5
Kowalski, P. M., & Saumon, D. 2006, ApJ, 651, L137
Lallement, R., Welsh, B. Y., Vergely, J. L., Crifo, F., & Sfeir, D. 2003, A&A, 411, 447
Lindegren, L., Hernández, J., Bombrun, A. et al. 2018, A&A, 616, A2 (*Gaia* 2 SI)
Liu, F., Yong, D., Asplund, M., Ramírez, I., & Meléndez, J. 2016, MNRAS, 457, 3934
Loktin, A. V., & Beshenov, G. V. 2003, Astron. Rep., 47, 6
Luri, X., Brown, A. G. A., Sarro, L., et al. 2018, A&A, 616, A9 (*Gaia* 2 SI)
Marigo, P., Girardi, L., Bressan, A., et al. 2017, ApJ, 835, 77
Marino, A. F., Milone, A. P., Przybilla, N., et al. 2014, MNRAS, 437, 1609
Marrese, P., Marinoni, S., Fabrizio, M., & Altavilla, G. 2018, A&A, submitted (*Gaia* 2 SI)
Michaud, G., Richard, O., Richer, J., & VandenBerg, D. A. 2004, ApJ, 606, 452
Miglio, A., Brogaard, K., & Handberg, R. 2015, IAU General Assembly, 22, 2251619
Milone, A. P., Piotto, G., Bedin, L. R., et al. 2012, ApJ, 744, 58
Moraux, E., Bouvier, J., Stauffer, J. R., Barrado y Navascués, D., & Cuillandre, J.-C. 2007, A&A, 471, 499
Mucciarelli, A., Dalessandro, E., Massari, D., et al. 2016, ApJ, 824, 73
Netopil, M., Paunzen, E., & Carraro, G. 2015, A&A, 582, A19
Netopil, M., Paunzen, E., Heiter, U., & Soubiran, C. 2016, A&A, 585, A150
Nissen, P. E., & Schuster, W. J. 2010, A&A, 511, L10
Parsons, S. G., Gänsicke, B. T., Marsh, T. R., et al. 2017, MNRAS, 470, 4473
Pasetto, S., Chiosi, C., Chiosi, E., Cropper, M., & Weiss, A. 2016, MNRAS, 459, 3182
Perryman, M. A. C., Lindegren, L., Kovalevsky, J., et al. 1995, A&A, 304, 69
Posti, L., Helmi, A., Veljanoski, J., & Breddels, M. 2018, A&A, 615, A70
Powalka, M., Lançon, A., Puzia, T. H., et al. 2017, ApJ, 844, 104
Provencal, J. L., Shipman, H. L., Høg, E., & Thejll, P. 1998, ApJ, 494, 759
Ruiz-Dern, L., Babusiaux, C., Arenou, F., Turon, C., & Lallement, R. 2018, A&A, 609, A116
Salaris, M., Chieffi, A., & Straniero, O. 1993, ApJ, 414, 580
Sartoretti, P., Katz, D., Cropper, M., et al. 2018, A&A, 616, A6 (*Gaia* 2 SI)
Saumon, D., & Marley, M. S. 2008, ApJ, 689, 1327
Schlegel, D. J., Finkbeiner, D. P., & Davis, M. 1998, ApJ, 500, 525
Skrutskie, M. F., Cutri, R. M., Stiening, R., et al. 2006, AJ, 131, 1163
Smart, R. L., Marocco, F., Caballero, J. A., et al. 2017, MNRAS, 469, 401
Stello, D., Vanderburg, A., Casagrande, L., et al. 2016, ApJ, 832, 133
Szczerba, R., Siódmiak, N., Stasińska, G., & Borkowski, J. 2007, A&A, 469, 799
Taylor, B. J. 2007, AJ, 133, 370
Tremblay, P.-E., Ludwig, H.-G., Steffen, M., Bergeron, P., & Freytag, B. 2011, A&A, 531, L19
Tremblay, P.-E., Gentile-Fusillo, N., Raddi, R., et al. 2017, MNRAS, 465, 2849
Valcarce, A. A. R., Catelan, M., Alonso-García, J., Contreras Ramos, R., & Alves, S. 2016, A&A, 589, A126
van Leeuwen, F. 2009, A&A, 497, 209
Weiss, A., & Heners, N. 2013, Eur. Phys. J. Web Conf., 43, 01002
Zinn, R. 1985, ApJ, 293, 424

[1] Université Grenoble Alpes, CNRS, IPAG, 38000 Grenoble, France
[2] GEPI, Observatoire de Paris, Université PSL, CNRS, 5 Place Jules Janssen, 92190 Meudon, France
[3] Institute of Astronomy, University of Cambridge, Madingley Road, Cambridge CB3 0HA, UK

[4] Leicester Institute of Space and Earth Observation and Department of Physics and Astronomy, University of Leicester, University Road, Leicester LE1 7RH, UK
[5] Institut de Ciències del Cosmos, Universitat de Barcelona (IEEC-UB), Martí i Franquès 1, 08028 Barcelona, Spain
[6] INAF – Osservatorio astronomico di Padova, Vicolo Osservatorio 5, 35122 Padova, Italy
[7] SISSA – Scuola Internazionale Superiore di Studi Avanzati, via Bonomea 265, 34136 Trieste, Italy
[8] Leiden Observatory, Leiden University, Niels Bohrweg 2, 2333 CA Leiden, The Netherlands
[9] Science Support Office, Directorate of Science, European Space Research and Technology Centre (ESA/ESTEC), Keplerlaan 1, 2201 AZ Noordwijk, The Netherlands
[10] Max Planck Institute for Astronomy, Königstuhl 17, 69117 Heidelberg, Germany
[11] Astronomisches Rechen-Institut, Zentrum für Astronomie der Universität Heidelberg, Mönchhofstr. 12-14, 69120 Heidelberg, Germany
[12] Department of Astronomy, University of Geneva, Chemin des Maillettes 51, 1290 Versoix, Switzerland
[13] Mission Operations Division, Operations Department, Directorate of Science, European Space Research and Technology Centre (ESA/ESTEC), Keplerlaan 1, 2201 AZ Noordwijk, The Netherlands
[14] Lohrmann Observatory, Technische Universität Dresden, Mommsenstraße 13, 01062 Dresden, Germany
[15] European Space Astronomy Centre (ESA/ESAC), Camino bajo del Castillo s/n, Urbanización Villafranca del Castillo, Villanueva de la Cañada, 28692 Madrid, Spain
[16] Lund Observatory, Department of Astronomy and Theoretical Physics, Lund University, Box 43, 22100 Lund, Sweden
[17] Université Côte d'Azur, Observatoire de la Côte d'Azur, CNRS, Laboratoire Lagrange, Bd de l'Observatoire, CS 34229, 06304 Nice Cedex 4, France
[18] CNES Centre Spatial de Toulouse, 18 avenue Edouard Belin, 31401 Toulouse Cedex 9, France
[19] Institut d'Astronomie et d'Astrophysique, Université Libre de Bruxelles CP 226, Boulevard du Triomphe, 1050 Bruxelles, Belgium
[20] F.R.S.-FNRS, Rue d'Egmont 5, 1000 Bruxelles, Belgium
[21] INAF – Osservatorio Astrofisico di Arcetri, Largo Enrico Fermi 5, 50125 Firenze, Italy
[22] Telespazio Vega UK Ltd for ESA/ESAC, Camino bajo del Castillo s/n, Urbanización Villafranca del Castillo, Villanueva de la Cañada, 28692 Madrid, Spain
[23] Laboratoire d'astrophysique de Bordeaux, Univ. Bordeaux, CNRS, B18N, allée Geoffroy Saint-Hilaire, 33615 Pessac, France
[24] Mullard Space Science Laboratory, University College London, Holmbury St Mary, Dorking, Surrey RH5 6NT, UK
[25] INAF – Osservatorio Astrofisico di Torino, via Osservatorio 20, 10025 Pino Torinese, Italy
[26] INAF – Osservatorio di Astrofisica e Scienza dello Spazio di Bologna, via Piero Gobetti 93/3, 40129 Bologna, Italy
[27] Serco Gestión de Negocios for ESA/ESAC, Camino bajo del Castillo s/n, Urbanización Villafranca del Castillo, Villanueva de la Cañada, 28692 Madrid, Spain
[28] ALTEC SpA, Corso Marche 79, 10146 Torino, Italy
[29] Department of Astronomy, University of Geneva, Chemin d'Ecogia 16, 1290 Versoix, Switzerland
[30] Gaia DPAC Project Office, ESAC, Camino bajo del Castillo s/n, Urbanización Villafranca del Castillo, Villanueva de la Cañada, 28692 Madrid, Spain
[31] SYRTE, Observatoire de Paris, Université PSL, CNRS, Sorbonne Université, LNE, 61 avenue de l'Observatoire 75014 Paris, France
[32] National Observatory of Athens, I. Metaxa and Vas. Pavlou, Palaia Penteli, 15236 Athens, Greece
[33] IMCCE, Observatoire de Paris, Université PSL, CNRS, Sorbonne Université, Univ. Lille, 77 av. Denfert-Rochereau, 75014 Paris, France
[34] Royal Observatory of Belgium, Ringlaan 3, 1180 Brussels, Belgium
[35] Institute for Astronomy, University of Edinburgh, Royal Observatory, Blackford Hill, Edinburgh EH9 3HJ, UK
[36] Instituut voor Sterrenkunde, KU Leuven, Celestijnenlaan 200D, 3001 Leuven, Belgium
[37] Institut d'Astrophysique et de Géophysique, Université de Liège, 19c Allée du 6 Août, B-4000 Liège, Belgium
[38] ATG Europe for ESA/ESAC, Camino bajo del Castillo s/n, Urbanización Villafranca del Castillo, Villanueva de la Cañada, 28692 Madrid, Spain
[39] Área de Lenguajes y Sistemas Informáticos, Universidad Pablo de Olavide, Ctra. de Utrera, km 1. 41013 Sevilla, Spain
[40] ETSE Telecomunicación, Universidade de Vigo, Campus Lagoas-Marcosende, 36310 Vigo, Spain
[41] Large Synoptic Survey Telescope, 950 N. Cherry Avenue, Tucson, AZ 85719, USA
[42] Observatoire Astronomique de Strasbourg, Université de Strasbourg, CNRS, UMR 7550, 11 rue de l'Université, 67000 Strasbourg, France
[43] Kavli Institute for Cosmology, University of Cambridge, Madingley Road, Cambride CB3 0HA, UK
[44] Aurora Technology for ESA/ESAC, Camino bajo del Castillo s/n, Urbanización Villafranca del Castillo, Villanueva de la Cañada, 28692 Madrid, Spain
[45] Laboratoire Univers et Particules de Montpellier, Université Montpellier, Place Eugène Bataillon, CC72, 34095 Montpellier Cedex 05, France
[46] Department of Physics and Astronomy, Division of Astronomy and Space Physics, Uppsala University, Box 516, 75120 Uppsala, Sweden
[47] CENTRA, Universidade de Lisboa, FCUL, Campo Grande, Edif. C8, 1749-016 Lisboa, Portugal
[48] Università di Catania, Dipartimento di Fisica e Astronomia, Sezione Astrofisica, Via S. Sofia 78, 95123 Catania, Italy
[49] INAF – Osservatorio Astrofisico di Catania, via S. Sofia 78, 95123 Catania, Italy
[50] Department of Astrophysics, University of Vienna, Türkenschanzstraße 17, A1180 Vienna, Austria
[51] CITIC – Department of Computer Science, University of A Coruña, Campus de Elviña s/n, 15071, A Coruña, Spain
[52] CITIC – Astronomy and Astrophysics, University of A Coruña, Campus de Elviña s/n, 15071, A Coruña, Spain
[53] INAF – Osservatorio Astronomico di Roma, Via di Frascati 33, 00078 Monte Porzio Catone, Italy
[54] Space Science Data Center – ASI, Via del Politecnico SNC, 00133 Roma, Italy
[55] Department of Physics, University of Helsinki, P.O. Box 64, 00014 Helsinki, Finland
[56] Finnish Geospatial Research Institute FGI, Geodeetinrinne 2, 02430 Masala, Finland
[57] Isdefe for ESA/ESAC, Camino bajo del Castillo s/n, Urbanización Villafranca del Castillo, Villanueva de la Cañada, 28692 Madrid, Spain
[58] Institut UTINAM UMR6213, CNRS, OSU THETA Franche-Comté Bourgogne, Université Bourgogne Franche-Comté, 25000 Besançon, France
[59] STFC, Rutherford Appleton Laboratory, Harwell, Didcot OX11 0QX, UK
[60] Departamento de Inteligencia Artificial, UNED, c/ Juan del Rosal 16, 28040 Madrid, Spain
[61] Elecnor Deimos Space for ESA/ESAC, Camino bajo del Castillo s/n, Urbanización Villafranca del Castillo, Villanueva de la Cañada, 28692 Madrid, Spain
[62] Thales Services for CNES Centre Spatial de Toulouse, 18 avenue Edouard Belin, 31401 Toulouse Cedex 9, France
[63] Department of Astrophysics/IMAPP, Radboud University, PO Box 9010, 6500 GL Nijmegen, The Netherlands
[64] European Southern Observatory, Karl-Schwarzschild-Str. 2, 85748 Garching, Germany

[65] ON/MCTI-BR, Rua Gal. José Cristino 77, Rio de Janeiro, CEP 20921-400, Brazil
[66] OV/UFRJ-BR, Ladeira Pedro Antônio 43, Rio de Janeiro, CEP 20080-090, Brazil
[67] Department of Terrestrial Magnetism, Carnegie Institution for Science, 5241 Broad Branch Road, NW, Washington, DC 20015-1305, USA
[68] Università di Torino, Dipartimento di Fisica, via Pietro Giuria 1, 10125 Torino, Italy
[69] Departamento de Astrofísica, Centro de Astrobiología (CSIC-INTA), ESA-ESAC, Camino Bajo del Castillo s/n, 28692 Villanueva de la Cañada, Madrid, Spain
[70] Departamento de Estadística, Universidad de Cádiz, Calle República Árabe Saharawi s/n, 11510 Puerto Real, Spain
[71] Astronomical Institute Bern University, Sidlerstrasse 5, 3012 Bern, Switzerland (present address)
[72] EURIX S.r.l., Corso Vittorio Emanuele II 61, 10128 Torino, Italy
[73] Harvard-Smithsonian Center for Astrophysics, 60 Garden Street, Cambridge MA 02138, USA
[74] HE Space Operations BV for ESA/ESAC, Camino bajo del Castillo s/n, Urbanización Villafranca del Castillo, Villanueva de la Cañada, 28692 Madrid, Spain
[75] Kapteyn Astronomical Institute, University of Groningen, Landleven 12, 9747 AD Groningen, The Netherlands
[76] Department of Computer Sciences, University of Turin, Corso Svizzera 185, 10149 Torino, Italy
[77] SRON, Netherlands Institute for Space Research, Sorbonnelaan 2, 3584CA Utrecht, The Netherlands
[78] Departamento de Matemática Aplicada y Ciencias de la Computación, Universidad de Cantabria, ETS Ingenieros de Caminos, Canales y Puertos, Avda. de los Castros s/n, 39005 Santander, Spain
[79] Unidad de Astronomía, Universidad de Antofagasta, Avenida Angamos 601, Antofagasta 1270300, Chile
[80] CRAAG – Centre de Recherche en Astronomie, Astrophysique et Géophysique, Route de l'Observatoire Bp 63 Bouzareah 16340 Alger, Algeria
[81] University of Antwerp, Onderzoeksgroep Toegepaste Wiskunde, Middelheimlaan 1, 2020 Antwerp, Belgium
[82] INAF – Osservatorio Astronomico d'Abruzzo, Via Mentore Maggini, 64100 Teramo, Italy
[83] INAF – Osservatorio Astronomico di Capodimonte, Via Moiariello 16, 80131 Napoli, Italy
[84] Instituto de Astronomia, Geofìsica e Ciências Atmosféricas, Universidade de São Paulo, Rua do Matão 1226, Cidade Universitaria, 05508-900 São Paulo, Brazil
[85] Department of Astrophysics, Astronomy and Mechanics, National and Kapodistrian University of Athens, Panepistimiopolis, Zografos, 15783 Athens, Greece
[86] Leibniz Institute for Astrophysics Potsdam (AIP), An der Sternwarte 16, 14482 Potsdam, Germany
[87] RHEA for ESA/ESAC, Camino bajo del Castillo s/n, Urbanización Villafranca del Castillo, Villanueva de la Cañada, 28692 Madrid, Spain
[88] ATOS for CNES Centre Spatial de Toulouse, 18 avenue Edouard Belin, 31401 Toulouse Cedex 9, France
[89] School of Physics and Astronomy, Tel Aviv University, Tel Aviv 6997801, Israel
[90] UNINOVA – CTS, Campus FCT-UNL, Monte da Caparica, 2829-516 Caparica, Portugal
[91] School of Physics, O'Brien Centre for Science North, University College Dublin, Belfield, Dublin 4, Ireland
[92] Dipartimento di Fisica e Astronomia, Università di Bologna, Via Piero Gobetti 93/2, 40129 Bologna, Italy
[93] Barcelona Supercomputing Center – Centro Nacional de Supercomputación, c/ Jordi Girona 29, Ed. Nexus II, 08034 Barcelona, Spain
[94] Department of Computer Science, Electrical and Space Engineering, Luleå University of Technology, Box 848, S-981 28 Kiruna, Sweden
[95] Max Planck Institute for Extraterrestrial Physics, High Energy Group, Gießenbachstraße, 85741 Garching, Germany
[96] Astronomical Observatory Institute, Faculty of Physics, Adam Mickiewicz University, Słoneczna 36, 60-286 Poznań, Poland
[97] Konkoly Observatory, Research Centre for Astronomy and Earth Sciences, Hungarian Academy of Sciences, Konkoly Thege Miklós út 15-17, 1121 Budapest, Hungary
[98] Eötvös Loránd University, Egyetem tér 1-3, H-1053 Budapest, Hungary
[99] American Community Schools of Athens, 129 Aghias Paraskevis Ave. & Kazantzaki Street, Halandri, 15234 Athens, Greece
[100] Faculty of Mathematics and Physics, University of Ljubljana, Jadranska ulica 19, 1000 Ljubljana, Slovenia
[101] Villanova University, Department of Astrophysics and Planetary Science, 800 E Lancaster Avenue, Villanova PA 19085, USA
[102] Physics Department, University of Antwerp, Groenenborgerlaan 171, 2020 Antwerp, Belgium
[103] McWilliams Center for Cosmology, Department of Physics, Carnegie Mellon University, 5000 Forbes Avenue, Pittsburgh, PA 15213, USA
[104] Astronomical Institute, Academy of Sciences of the Czech Republic, Fričova 298, 25165 Ondřejov, Czech Republic
[105] Telespazio for CNES Centre Spatial de Toulouse, 18 avenue Edouard Belin, 31401 Toulouse Cedex 9, France
[106] Institut de Physique de Rennes, Université de Rennes 1, 35042 Rennes, France
[107] Shanghai Astronomical Observatory, Chinese Academy of Sciences, 80 Nandan Rd, 200030 Shanghai, PR China
[108] School of Astronomy and Space Science, University of Chinese Academy of Sciences, Beijing 100049, PR China
[109] Niels Bohr Institute, University of Copenhagen, Juliane Maries Vej 30, 2100 Copenhagen Ø, Denmark
[110] DXC Technology, Retortvej 8, 2500 Valby, Denmark
[111] Las Cumbres Observatory, 6740 Cortona Drive Suite 102, Goleta, CA 93117, USA
[112] Astrophysics Research Institute, Liverpool John Moores University, 146 Brownlow Hill, Liverpool L3 5RF, UK
[113] Baja Observatory of University of Szeged, Szegedi út III/70, 6500 Baja, Hungary
[114] Laboratoire AIM, IRFU/Service d'Astrophysique – CEA/DSM – CNRS – Université Paris Diderot, Bât. 709, CEA-Saclay, 91191 Gif-sur-Yvette Cedex, France
[115] Warsaw University Observatory, Al. Ujazdowskie 4, 00-478 Warszawa, Poland
[116] Faculty of Mathematics and Physics, Institute of Theoretical Physics, Charles University, Prague, Czech Republic
[117] AKKA for CNES Centre Spatial de Toulouse, 18 avenue Edouard Belin, 31401 Toulouse Cedex 9, France
[118] Vitrociset Belgium for ESA/ESAC, Camino bajo del Castillo s/n, Urbanización Villafranca del Castillo, Villanueva de la Cañada, 28692 Madrid, Spain
[119] HE Space Operations BV for ESA/ESTEC, Keplerlaan 1, 2201 AZ Noordwijk, The Netherlands
[120] Space Telescope Science Institute, 3700 San Martin Drive, Baltimore MD 21218, USA
[121] QUASAR Science Resources for ESA/ESAC, Camino bajo del Castillo s/n, Urbanización Villafranca del Castillo, Villanueva de la Cañada, 28692 Madrid, Spain
[122] Fork Research, Rua do Cruzado Osberno, Lt. 1, 9 esq., Lisboa, Portugal
[123] APAVE SUDEUROPE SAS for CNES Centre Spatial de Toulouse, 18 avenue Edouard Belin, 31401 Toulouse Cedex 9, France
[124] Nordic Optical Telescope, Rambla José Ana Fernández Pérez 7, 38711 Breña Baja, Spain
[125] Spanish Virtual Observatory, Spain
[126] Fundación Galileo Galilei – INAF, Rambla José Ana Fernández Pérez 7, 38712 Breña Baja, Santa Cruz de Tenerife, Spain

[127] INSA for ESA/ESAC, Camino bajo del Castillo s/n, Urbanización Villafranca del Castillo, Villanueva de la Cañada, 28692 Madrid, Spain
[128] Departamento de Arquitectura de Computadores y Automática, Facultad de Informática, Universidad Complutense de Madrid, C/ Prof. José García Santesmases s/n, 28040 Madrid, Spain
[129] H H Wills Physics Laboratory, University of Bristol, Tyndall Avenue, Bristol BS8 1TL, UK
[130] Institut d'Estudis Espacials de Catalunya (IEEC), Gran Capita 2-4, 08034 Barcelona, Spain
[131] Applied Physics Department, Universidade de Vigo, 36310 Vigo, Spain
[132] Stellar Astrophysics Centre, Aarhus University, Department of Physics and Astronomy, 120 Ny Munkegade, Building 1520, DK-8000 Aarhus C, Denmark
[133] Argelander-Institut für Astronomie, Universität Bonn, Auf dem Hügel 71, 53121 Bonn, Germany
[134] Research School of Astronomy and Astrophysics, Australian National University, Canberra, ACT 2611 Australia
[135] Sorbonne Universités, UPMC Univ. Paris 6 et CNRS, UMR 7095, Institut d'Astrophysique de Paris, 98 bis bd. Arago, 75014 Paris, France
[136] Department of Geosciences, Tel Aviv University, Tel Aviv 6997801, Israel

Table A.1. Membership data for the open clusters.

DR2 SourceId	cluster	α (degr)	δ (degr)	ϖ_d mas	$\sigma\varpi_d$ mas
685747814353991296	Praesepe	133.15933	21.15502	5.645	0.033
685805259540481664	Praesepe	133.57003	21.73443	4.798	0.100
665141141087298688	Praesepe	130.22501	21.75663	5.630	0.020
...	...	...	...	...	...

Notes. Only the first three lines with data for members of the Praesepe cluster are presented here. For the more distant clusters, the last two columns are not included. The astrometric and photometric extra filters presented in Sect. 2.1 and used in the figures of this paper are not applied in this table. The full table will be available in electronic form at the CDS.

Appendix A: Open cluster membership and astrometric solutions

A.1. Nearby clusters

The nearby clusters were analysed with the method described and applied to the Hyades cluster in the first *Gaia* data release (Gaia Collaboration 2017). By combining the information from the measured proper motions and parallaxes for individual cluster members, it is possible to derive a higher precision measurement for the relative parallax of these cluster members. The proper motion observed for an individual cluster member represents the local projection on the sky of the baricentric velocity of the cluster. It is therefore affected by the angular separation on the sky of the member star from the projection of the cluster centre and the baricentric distance of the star, again relative to that of the cluster centre. Similarly, the measured parallax for the star can be significantly different from the mean parallax of the cluster.

The primary aim of the present paper is to provide high-precision HRDs, for which these accurate relative parallaxes contribute important information by reducing the actual differential distance modulus variations of cluster members. The effectiveness of this procedure is limited by the amplitude of the proper motion of the cluster centre and the ratio of the diameter over the distance of the cluster. The standard uncertainties in the individual parallaxes and proper motions of the cluster members in the second *Gaia* data release allow for this procedure to be applied for clusters within 250 pc. Table A.1 shows an example of an extract from the cluster member files produced for each of the nine clusters treated in this way.

Nine clusters within 250 pc from the Sun were analysed as nearby clusters. The analysis is iterative, and consists of two elements: 1. determinations of the space velocity vector at the cluster centre, and 2. determination of the cluster centre. A first selection is made of stars contained in a sphere with a radius of around 15 pc around the assumed centre of the cluster. A summary of the observed radii for the nearby and more distant clusters is shown in Fig. A.1. The radius can be adjusted based on the derived surface density distribution (Fig. A.2), where the outermost radius is set at the point beyond which the density of contaminating field stars starts to dominate. The selected stars are further filtered on their agreement between the observed proper motion and the predicted projection of the assumed space motion at the 3D position of the star, using the measured stellar parallax, and taking into account the uncertainties on the observed proper motion and parallax. The solution for the space motion follows Eq. A13 in Gaia Collaboration (2017). Although it is in principle possible to solve also for the radial velocity

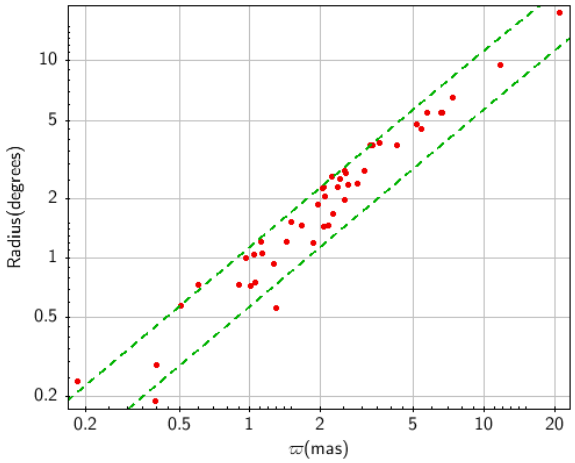

Fig. A.1. Maximum radius in degrees in DR2 for the 46 open clusters as a function of parallax. The two diagonal lines represent maximum radii of 10 (*bottom*) and 20 (*top*) pc.

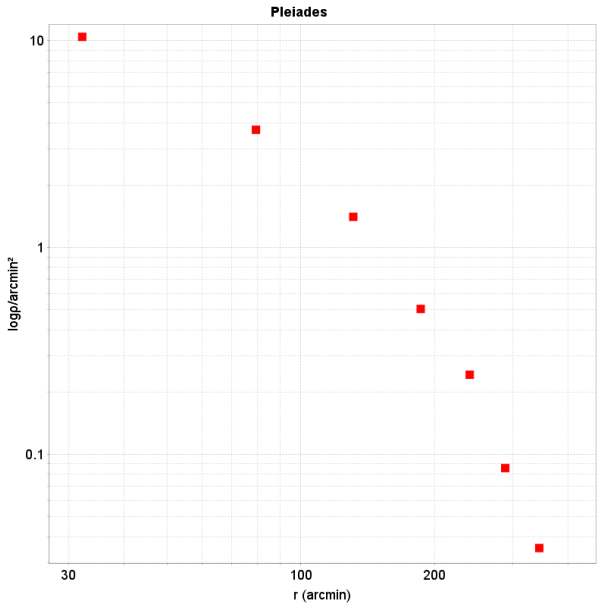

Fig. A.2. Surface-density profile for the Pleiades cluster, based on 1332 identified cluster members.

using only the astrometric data, this effectively only works for the Hyades cluster. Instead, a single equation for the observed radial velocity of the cluster was added, where the observed radial velocity is based on the weighted mean of the *Gaia* radial velocities of cluster members for which these data are available.

To stabilise the solution, it is important to align the coordinate system with the line of sight towards the cluster centre, minimising the mixing of the contributions from the proper motions and the additional information from the radial velocity. The solution for the space motion does provide an estimate of the radial velocity component, but except for the Hyades and Coma Ber, this is largely dominated by the radial velocity value and its accuracy that is used as input to the solution. Small differences are therefore seen between the radial velocities as presented in Table A.2 (as directly derived from the *Gaia* spectroscopic data) and in Table A.3 (the summary data for the nine clusters in this selection), where the astrometric information on the radial velocity is also taken into account. Figure A.3 shows an example of the level of agreement between the differential

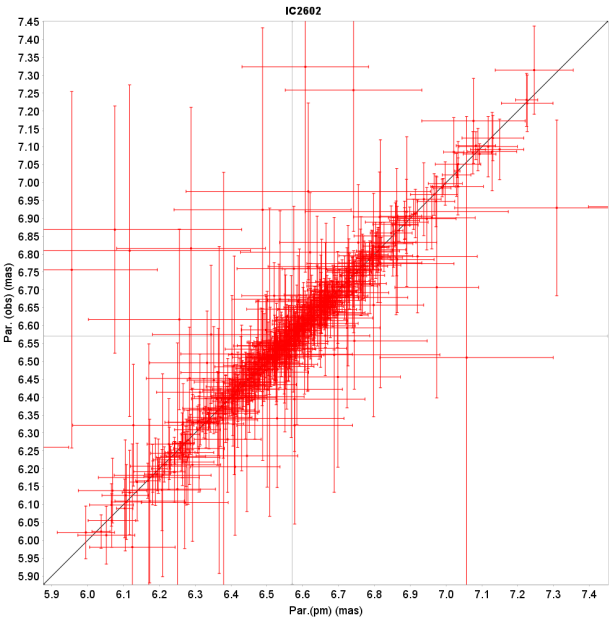

Fig. A.3. Comparison between the directly measured parallaxes and the parallaxes obtained by including the relative proper motion data, for the cluster IC 2602. The clear linear relation shows the good agreement between proper motion and parallax offsets from the mean cluster values.

Table A.2. Mean radial velocity values as derived from the *Gaia* spectroscopic data for nearby clusters.

Name	$V_{\rm rad}$	$\sigma(V_{\rm rad})$	uwsd	Nobs
Hyades	39.87	0.05	2.28	150
ComaBer	0.21	0.13	2.15	43
Pleiades	5.54	0.10	2.00	195
IC2391	15.00	0.24	1.19	35
IC2602	17.62	0.22	1.24	36
alphaPer	−0.32	0.17	1.38	71
Praesepe	34.84	0.07	1.45	176
NGC2451A	23.08	0.34	1.32	31
Blanco1	6.01	0.15	1.03	51

Notes. Columns: 1. Cluster name; 2: weighted-mean radial velocity in km s^{-1}; 3. standard uncertainty on radial velocity; 4. unit-weight standard deviation of mean velocity solution; and 5. number of observations in mean velocity solution.

parallax and proper motion values in the cluster IC 2602. In Fig. A.4 we also show an example of the 3D distribution maps for this cluster; maps like this were prepared for all nearby clusters.

Next to the astrometric data, the second *Gaia* data release also presents radial velocity measurements for a magnitude-limited sample. The radial velocities were compared with the projection of the cluster space velocity at the position of each star for which these data are available. This is particularly relevant for stars in the Hyades cluster, where the projection effects of the radial velocity can be of the order of several km s^{-1}. Table A.2 presents the results for the nine nearby clusters.

Figure A.5 shows the differences (observed − predicted, where the predicted value is based on the local projection of the space velocity of the cluster) in the radial velocities for 191 stars in the Hyades cluster. Only stars for which the colour index $G_{\rm BP} - G_{\rm RP}$ is greater than 0.4 mag were used. The results for all 9 nearby clusters are shown in Table A.2.

A.2. More distant open clusters

For the more distant clusters, a selection was made of 37 relatively rich clusters, generally only little reddened, and as far as possible, covering a spread in ages and chemical composition (Fig. A.6). These clusters were all analysed in a combined solution of the mean parallax and proper motion from the observed astrometric data of the member stars. This is an iterative procedure, where cluster membership determination is based on the solution for the astrometric parameters of the cluster. The combined solution for the astrometric parameters of a cluster takes into account noise contributions from three sources:

1. the covariance matrix of the astrometric solution for each star;
2. the internal velocity dispersion of the cluster, affecting the dispersion of the proper motions;
3. the effect of the cluster size relative to its distance, which
   (a) is reflected in a dispersion on the parallaxes of the cluster members;
   (b) is reflected in a dispersion in proper motions in the direction of, and scaled by, the cluster proper motion.

When we assume that the velocity distribution is isotropic within the measurement accuracy, then the second of these noise contributions will be diagonal. The first and third may also contain significant off-diagonal elements. Given a cluster parallax of ϖ_c, a cluster proper motion of $(\mu_{\alpha,c}, \mu_{\delta,c})$, and an average relative dispersion in the parallaxes of the cluster stars of $\sigma_\varpi/\varpi = \sigma_R/R$ (where R is the distance to the cluster centre), the contribution to the dispersion in the proper motions of the cluster stars scales with the relative dispersion of the parallaxes and the proper motions of the cluster:

$$\sigma\mu_{\alpha,s} = |\mu_{\alpha,c}| \times \sigma_\varpi/\varpi \quad \text{(A.1)}$$

$$\sigma\mu_{\delta,s} = |\mu_{\delta,c}| \times \sigma_\varpi/\varpi. \quad \text{(A.2)}$$

For most of the clusters with distances beyond 250 pc, this contribution will be small to very small relative to other contributions. Figure A.7 shows the overall relation between parallaxe and proper motion amplitudes for the selection of clusters we used.

The contributions are summed into a single noise matrix, of which an upper-triangular square root is used to normalise the observation equations that describe the cluster proper motion and parallax as a function of the observed proper motions and parallaxes of the individual cluster members.

Table A.4 presents an overview of the astrometric solutions for 37 open clusters, with mean radial velocities when available in the *Gaia* data. We note that some clusters are not included in Table 2 because their colour-magnitude diagrams are too disturbed by interstellar extinction (see an illustration of the differential extinction effect in Fig. A.8). The proper motions are compared with those presented by Loktin & Beshenov (2003) in Fig. A.9, and they agree well overall, but there is also an indication that errors on the data presented in Loktin & Beshenov (2003) are underestimated. In the same figure the comparison between the parallaxes as derived from the DR2 data and parallax values derived from photometric distances as (mostly) presented in Kharchenko et al. (2005) are shown, and again generally agree well (see also the validation with more clusters in Arenou et al. 2018). The systematic difference of 0.029 mas, which can be observed for globular clusters (Gaia Collaboration 2018c), is too small to be noticed here (Fig. A.10), but the calibration noise on the DR2 parallaxes (0.025 mas), obtained in the same study, is significantly larger than the standard uncertainties

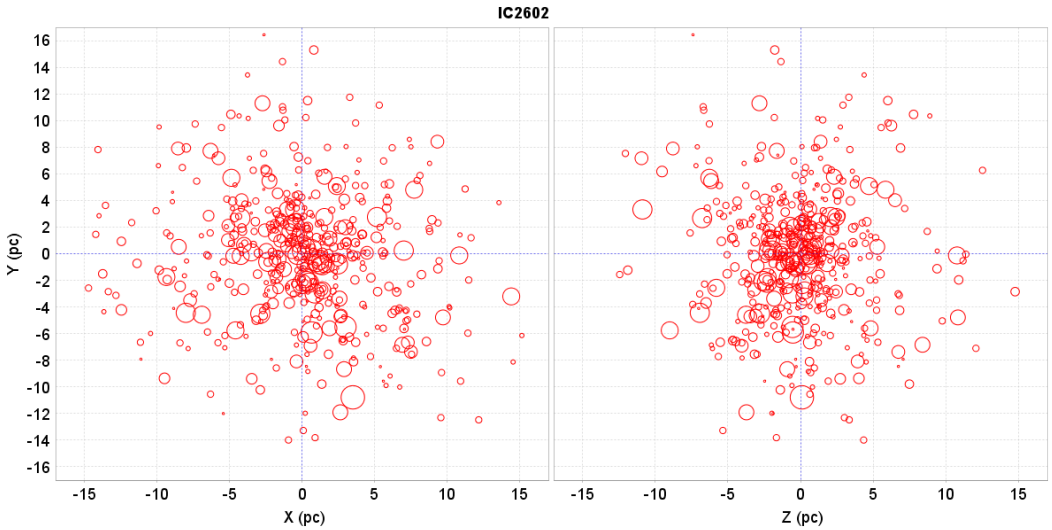

Fig. A.4. Distribution of stars in IC 2602 in galactic rectangular coordinates, showing the flattening in the Z (galactic pole) direction.

Table A.3. Space velocity fitting results for nearby clusters.

Name ClustId	U' σU' km/s	V' σV' km/s	W' σW' km/s	$c_{U'V'}$ $c_{V'W'}$	$c_{U'W'}$ σv	uwsd Observ.	α_c δ_c degr.	ϖ $\sigma\varpi$ mas	V_{rad} σV_{rad} km/s	$\mu_{\alpha*}$ $\sigma\mu_{\alpha*}$ mas/yr	μ_δ $\sigma\mu_\delta$ mas/yr
Hyades	−6.059	45.691	5.544	0.33	0.35	0.67	97.5407	21.052	39.96	101.005	−28.490
C0424+157	0.031	0.069	0.025	0.93	0.40	515	6.8148	0.065	0.06	0.171	0.137
ComaBer	−1.638	4.785	−3.528	0.35	−0.86	0.48	110.1896	11.640	−0.52	−12.111	−8.996
C1222+263	0.078	0.018	0.040	−0.39	0.40	153	−34.3206	0.034	0.07	0.048	0.121
Pleiades	−1.311	21.390	−24.457	0.48	0.50	0.77	93.5183	7.364	5.65	19.997	−45.548
C0344+239	0.070	0.105	0.057	0.90	0.40	1326	−48.7831	0.005	0.09	0.127	0.101
Praesepe	0.339	49.097	1.200	−0.50	−0.60	0.76	89.5122	5.371	35.64	−36.047	−12.917
C0937+201	0.090	0.106	0.050	0.92	0.40	938	1.3517	0.003	0.10	0.110	0.066
alphaPer	−5.110	24.183	−14.122	0.25	0.40	0.68	101.9183	5.718	−0.29	22.929	−25.556
C0318+484	0.053	0.067	0.097	0.59	0.40	740	−29.7555	0.005	0.08	0.071	0.095
IC2391	−0.751	28.459	−1.590	−0.20	0.38	0.68	91.6471	6.597	14.59	−24.927	23.256
C0838-528	0.054	0.062	0.105	−0.52	0.40	325	−3.4126	0.007	0.09	0.080	0.110
IC2602	−9.467	16.867	−12.377	−0.05	0.40	0.72	119.3285	6.571	17.43	−17.783	10.655
C1041-641	0.056	0.024	0.120	−0.16	0.40	492	−32.7371	0.007	0.11	0.040	0.098
Blanco1	6.176	21.150	−0.296	0.01	−0.86	0.65	73.6042	4.216	5.78	18.724	2.650
C0001-302	0.111	0.020	0.065	−0.02	0.40	489	−0.8388	0.003	0.10	0.017	0.070
NGC2451	5.806	32.440	−3.100	−0.24	0.34	0.68	79.8905	5.163	22.85	−21.063	15.378
C0743-378	0.048	0.095	0.084	−0.76	0.40	400	−5.4202	0.005	0.09	0.065	0.093

Notes. Columns: 1. Cluster identifiers; 2 to 4 U', V' and W' velocity components in the equatorial system; 5. U'V' error correlation (top) V'W' error correlation (bottom); 6. U'W' error correlation (top), applied internal velocity dispersion in km s^{-1} (bottom); 7. unit-weight standard deviation of solution (top), number of stars (bottom); 8. Coordinates of the convergent point; 9. parallax (mas); 10. radial velocity (km s^{-1}); 11. proper motion in right ascension; and 12. proper motion in declination.

on the mean cluster parallaxes and is therefore the main contributor to the uncertainties on the cluster parallaxes. In most cases, however, this amounts to less than 1% in error on the parallax, or 0.02 mag in distance modulus.

The maximum radius for each cluster was determined from the contrast between the cluster and the field stars in the proper motion and parallax domain. In practice, this means that the density of field stars for which the combined information on the parallax and proper motion, combined with uncertainties and error correlations, leaves a significant possibility for a field star to be a cluster member. When the surface density of these field stars becomes similar to the surface density of the cluster stars, we have reached the maximum radius for the cluster in this particular data set and parameter space. It is well possible, however, that for a catalogue with higher accuracies on the astrometric parameters for the fainter stars in particular, this limit will be found still farther away from the cluster centre. Radial velocities for the clusters, mostly as given in Kharchenko et al. (2005) or Conrad et al. (2014), were compared with the mean radial velocities as derived from the *Gaia* DR2 data. A limited spectral range was used, for which there is clear consistency of the radial velocity measurements. The summary of the results is shown in Fig. A.9 and generally agrees well (see also the validation with more clusters in Arenou et al. 2018). The largest discrepancies are found for NGC 2516 (RAVE measurements in Conrad et al. 2014) and Trumpler 2 (Kharchenko et al. 2005).

Table A.4. Overview of the results for open clusters with distances beyond 250 pc

Name ClustId	α δ deg	ϖ σ_ϖ mas	$\mu_{\alpha*}$ $\sigma_{\mu\alpha*}$ mas/yr	μ_δ $\sigma_{\mu\delta}$ mas/yr	c_{12} c_{13}	c_{23} r(max)$^\circ$	nMemb st.dev.	Vrad σ km s^{-1}	uwsd Obs.
NGC0188	11.7494	0.5053	−2.3087	−0.9565	−0.04	−0.02	1181	−41.86	1.43
C0039+850	85.2395	0.0011	0.0035	0.0030	0.16	0.58	0.84	0.13	20
NGC0752	29.2054	2.2304	9.8092	−11.7637	0.02	−0.04	433	5.90	1.68
C0154+374	37.7454	0.0027	0.0191	0.0180	0.04	2.58	0.86	0.11	76
Stock2	33.8282	2.6367	15.8241	−13.7669	0.01	0.01	1742	8.58	1.45
C0211+590	59.5813	0.0009	0.0103	0.0104	−0.00	2.36	0.78	0.09	109
NGC0869	34.7391	0.3942	−0.6943	−1.0831	0.14	0.10	829		
C0215+569	57.1339	0.0014	0.0038	0.0041	0.08	0.19	0.83		0
NGC0884	35.5430	0.3976	−0.6021	−1.0616	0.16	0.11	1077	−44.69	4.98
C0218+568	57.1591	0.0012	0.0035	0.0036	0.10	0.29	0.86	0.73	2
Trump02	39.1879	1.4316	1.5305	−5.3361	0.05	0.04	589	−4.06	0.75
C0233+557	55.8846	0.0023	0.0116	0.0117	0.01	1.21	0.90	0.09	4
NGC1039	40.5843	1.9536	0.7256	−5.7320	0.02	−0.02	764	−7.27	1.44
C0238+425	42.7027	0.0027	0.0109	0.0103	0.04	1.87	0.79	0.72	18
NGC1901	79.6838	2.3582	1.5953	12.6920	0.03	0.10	290	1.62	1.60
C0518-685	−68.1627	0.0031	0.0276	0.0277	−0.03	2.30	1.04	0.56	16
NGC2158	91.8751	0.1833	−0.1665	−1.9932	0.18	−0.19	3942	26.64	2.30
C0604+241	24.1163	0.0021	0.0035	0.0029	0.21	0.24	0.92	0.60	11
NGC2168	92.2688	1.1301	2.2784	−2.9336	0.08	−0.08	1794	−7.70	2.73
C0605+243	24.3148	0.0013	0.0052	0.0050	0.05	1.20	0.87	0.27	6
NGC2232	96.9973	3.0710	−4.7737	−1.9014	0.04	−0.04	318	24.22	0.96
C0624-047	−4.7929	0.0033	0.0185	0.0181	0.04	2.76	0.78	0.44	9
Trump10	131.8982	2.2637	−12.3536	6.5309	0.02	0.00	947	21.97	1.00
C0646-423	−42.5192	0.0014	0.0102	0.0104	−0.01	1.69	0.82	0.31	28
NGC2323	105.7245	1.0012	−0.7977	−0.6540	0.06	−0.03	382	11.55	
C0700-082	−8.3586	0.0017	0.0063	0.0063	0.00	0.73	0.87		1
NGC2360	109.4452	0.9018	0.3853	5.5893	0.07	−0.02	1037	28.02	1.74
C0715-155	−15.6317	0.0012	0.0048	0.0048	−0.05	0.74	0.79	0.19	15
Coll140	111.0308	2.5685	−8.1285	4.7105	0.02	0.02	332	18.53	1.75
C0722-321	−32.1113	0.0025	0.0215	0.0220	−0.01	2.69	0.81	1.85	5
NGC2423	114.2904	1.0438	−0.7343	−3.6333	0.09	−0.00	694	18.50	2.04
C0734-137	−13.8348	0.0017	0.0070	0.0069	−0.04	1.04	0.81	0.17	19
NGC2422	114.1463	2.0690	−7.0200	0.9592	0.05	0.01	907	36.21	1.42
C0734-143	−14.4844	0.0014	0.0098	0.0099	−0.02	1.45	0.74	0.57	30
NGC2437	115.4358	0.6005	−3.8232	0.3729	0.11	0.01	3032	37.34	
C0739-147	−14.8506	0.0009	0.0031	0.0031	−0.06	0.74	0.83		1
NGC2447	116.1262	0.9603	−3.5680	5.0434	0.03	0.01	926	22.37	3.01
C0742-237	−23.8567	0.0013	0.0056	0.0057	−0.01	1.00	0.80	0.26	11
NGC2516	119.5469	2.4118	−4.6579	11.1517	0.02	−0.00	2518	23.78	1.39
C0757-607	−60.7749	0.0006	0.0075	0.0075	−0.01	2.54	0.83	0.11	156
NGC2547	122.5654	2.5438	−8.5999	4.2542	0.02	0.00	644	15.46	2.47
C0809-491	−49.0498	0.0015	0.0148	0.0148	−0.00	2.79	0.78	0.83	22
NGC2548	123.3834	1.2897	−1.3302	1.0164	0.13	0.00	509	8.83	1.77
C0811-056	−5.7363	0.0024	0.0095	0.0093	−0.03	0.56	0.80	0.27	8
NGC2682	132.8476	1.1325	−10.9737	−2.9396	0.08	−0.00	1520	34.05	1.94
C0847+120	11.8369	0.0011	0.0064	0.0063	−0.01	1.06	0.76	0.10	66
NGC3228	155.3791	2.0323	−14.8800	−0.6498	0.03	0.03	222		
C1019-514	−51.7693	0.0029	0.0220	0.0220	−0.01	2.27	0.81		0
NGC3532	166.3975	2.0659	−10.3790	5.1958	0.03	−0.02	1879	4.85	2.24
C1104-584	−58.7335	0.0007	0.0079	0.0079	0.01	2.31	0.79	0.13	143
NGC6025	240.7714	1.2646	−2.8846	−3.0222	−0.02	0.01	452	−7.66	
C1559-603	−60.4562	0.0015	0.0100	0.0099	0.03	0.94	0.75		1
NGC6281	256.1638	1.8716	−1.8764	−3.9506	−0.03	0.05	573	−5.02	2.17
C1701-378	−37.9180	0.0019	0.0144	0.0136	0.05	1.19	0.80	0.20	21
IC4651	261.2035	1.0542	−2.4051	−5.0280	−0.07	0.10	960	−30.32	3.41
C1720-499	−49.9185	0.0014	0.0061	0.0060	0.06	0.76	0.80	0.19	56
NGC6405	265.1220	2.1626	−1.3662	−5.8063	−0.04	0.11	967	−9.20	5.39

Table A.4. continued.

Name ClustId	α δ deg	ϖ σ_ϖ mas	$\mu_{\alpha*}$ $\sigma_{\mu\alpha*}$ mas/yr	μ_δ $\sigma_{\mu\delta}$ mas/yr	c_{12} c_{13}	c_{23} r(max)°	nMemb st.dev.	Vrad σ km s^{-1}	uwsd Obs.
C1736-321	−32.4135	0.0021	0.0140	0.0132	0.04	1.46	0.82	0.77	17
IC4665	266.4978	2.8918	−0.8993	−8.5114	−0.02	0.04	174	−11.26	1.86
C1743+057	5.5653	0.0034	0.0347	0.0345	0.02	2.39	0.75	2.12	6
NGC6475	268.2736	3.5704	3.0722	−5.3157	−0.02	0.04	1140	−14.84	2.63
C1750-348	−34.6639	0.0016	0.0185	0.0184	0.02	3.86	0.82	0.17	113
NGC6633	276.8737	2.5232	1.1584	−1.7371	−0.03	0.09	321	−28.59	1.83
C1825+065	6.6081	0.0023	0.0199	0.0200	0.01	1.99	0.84	0.14	28
IC4725	277.9462	1.5043	−1.7201	−6.1010	−0.07	0.09	755		
C1828-192	−19.1058	0.0019	0.0091	0.0091	0.04	1.53	0.89		0
IC4756	279.6698	2.0943	1.2574	−4.9145	−0.04	0.06	543	−24.72	2.76
C1836+054	5.3836	0.0018	0.0134	0.0134	0.02	2.05	0.84	0.17	38
NGC6774	289.1055	3.2516	−0.9733	−26.6464	−0.03	0.11	234	41.79	3.36
C1913-163	−16.3901	0.0038	0.0367	0.0383	0.00	3.74	1.00	0.15	62
NGC6793	290.7795	1.6672	3.8120	3.5622	−0.03	0.06	465	−10.85	
C1921+220	22.1400	0.0021	0.0131	0.0136	−0.02	1.47	0.81		1
NGC7092	322.4220	3.3373	−7.3569	−19.5993	−0.02	−0.00	433	−5.07	0.95
C2130+482	48.1315	0.0024	0.0256	0.0260	−0.00	3.72	0.86	0.21	21

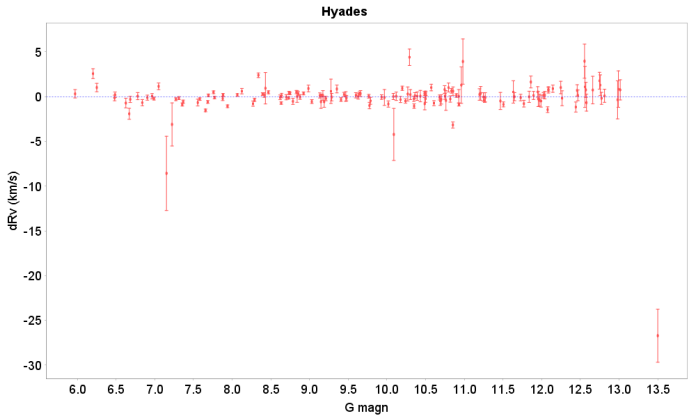

Fig. A.5. Differences between the predicted and observed radial velocities in the Hyades cluster as a function of G magnitude.

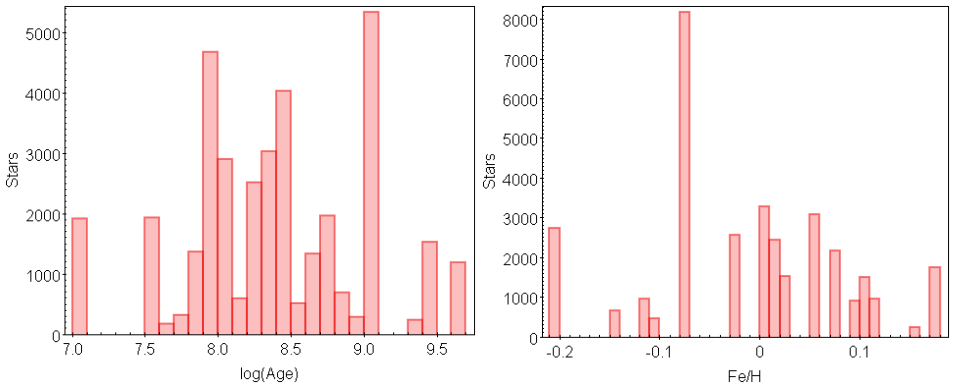

Fig. A.6. Distributions over age and composition for stars in the 32 open clusters selected for the composite HRD, including the nearby clusters.

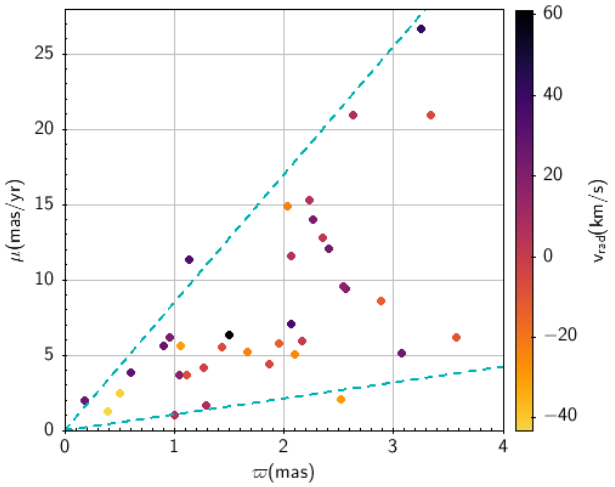

Fig. A.7. Comparison between the parallaxes and proper motions for the 37 open clusters. The upper and lower diagonal lines represent tangential velocities of 40 and 5 km s^{-1} , respectively.

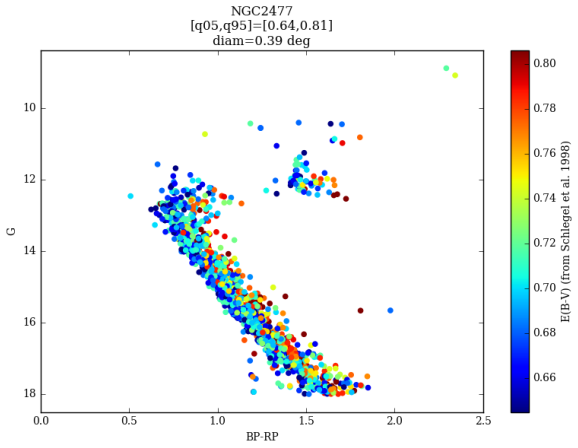

Fig. A.8. Colour-magnitude diagram of NGC 2477, with each star colour-coded by the value of integrated extinction in the catalogue of Schlegel et al. (1998).

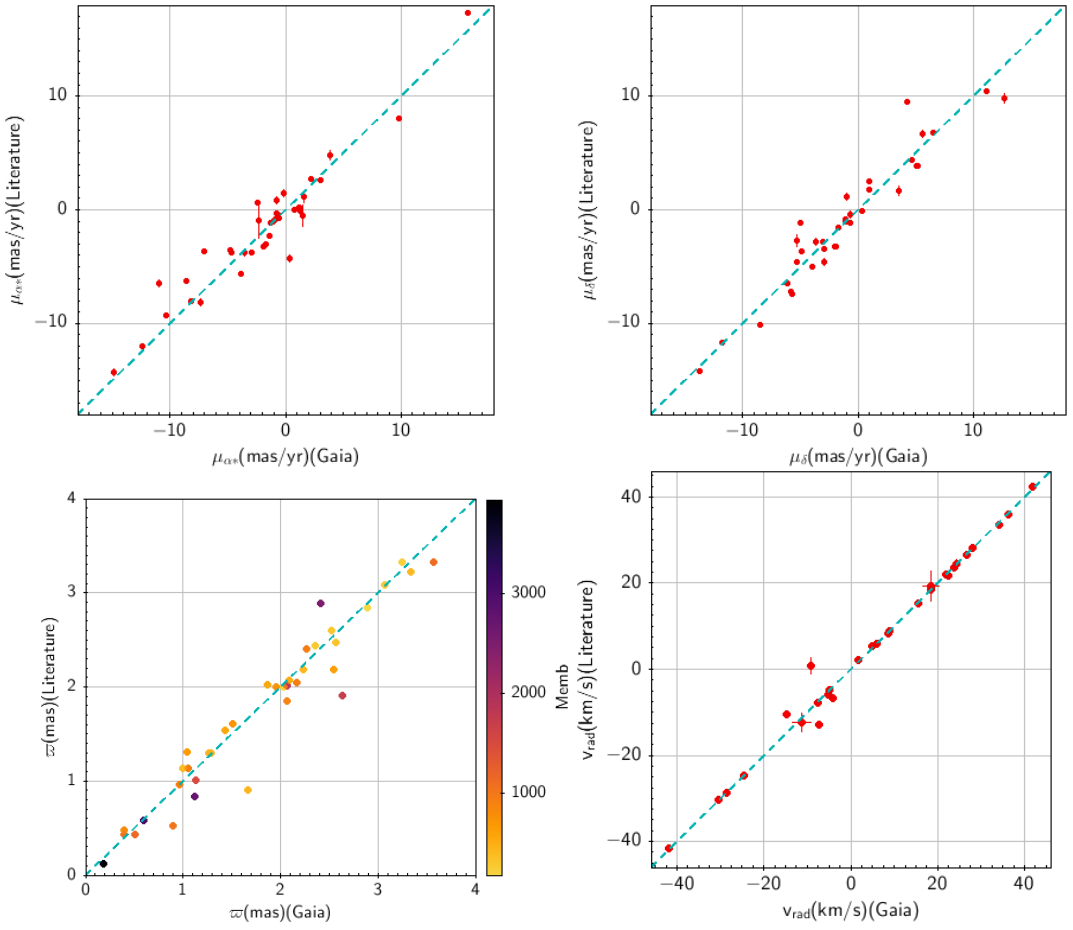

Fig. A.9. Comparisons with values quoted in literature (see text) for (*top*) proper motions in right ascension, proper motions in declination, (*bottom*) parallaxes, and radial velocities for 37 open clusters with distances beyond 250 pc.

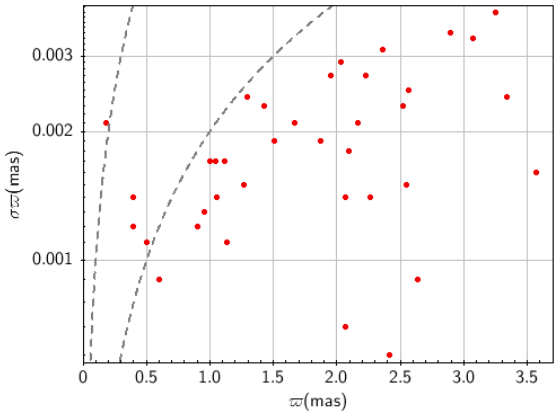

Fig. A.10. Standard uncertainties on the mean cluster parallax determinations. The curves represent the 100 and 500 σ significance levels when only the standard uncertainties are considered.

Appendix B: *Gaia* archive query

The *Gaia* archive[6] query corresponding to the filters described in Sect. 2.1 is the following (selecting here the first five stars):

```
SELECT TOP 5 phot_g_mean_mag+5*log10(parallax)-10 AS mg, bp_rp FROM gaiadr2.gaia_source
   WHERE parallax_over_error > 10
   AND phot_g_mean_flux_over_error>50
   AND phot_rp_mean_flux_over_error>20
   AND phot_bp_mean_flux_over_error>20
   AND phot_bp_rp_excess_factor < 1.3+0.06*power(phot_bp_mean_mag-phot_rp_mean_mag,2)
   AND phot_bp_rp_excess_factor > 1.0+0.015*power(phot_bp_mean_mag-phot_rp_mean_mag,2)
   AND visibility_periods_used>8
   AND astrometric_chi2_al/(astrometric_n_good_obs_al-5)<1.44*greatest(1,exp(-0.4*(phot_g_mean_mag-19.5)))
```

[6] https://gea.esac.esa.int/archive/